Memoirs of the Faculty of Science, Kyoto University, Series of Physics, Astrophysics, Geophysics and Chemistry, Vol. XXXVI, No. 3, Article 2, 1985

# Study of the Atomic Weight Dependence of High Pt Single Hadron Production in Proton-Nucleus Collisions at 400 GeV/c

By

**Yoshihide SAKAI***

Department of Physics, Faculty of Science, Kyoto University, Kyoto 606, Japan

(*Received June 8, 1984*)

**Abstract**

The atomic weight dependence of single high $P_t$ hadron productions in proton-nucleus collisions has been studied at an incident proton momentum of 400 Gev/c with the Be, Cu, and W targets. The measurements have been made in the range 3.5 to 8.0 Gev/c in $P_t$, and 70 to 110 degrees in polar angle in the center of momentum system of the proton and the target nucleon.

The results are compared with those of other experiments, and the relations to the $A$-dependence of other processes such as lepton-nucleus deep inelastic scattering are discussed using theoretical models.

## I. INTRODUCTION

High $P_t$ particle production is one of the "hard processes", as well as lepton-nucleon deep inelastic scattering and lepton pair production in hadron-nucleon collisions. "Hard process" implies that the momentum transfer $Q^2$ is much larger than the characteristic scale of hadrons such as hadron mass $M^2$. "Hard processes" are the most useful way to investigate the structure of hadrons, because processes with large momentum transfer involve collisions at small distance due to the uncertainty principle. In fact, starting from the pioneer work on electron-nucleon deep inelastic scattering at the Stanford Linear Accelerator Center (SLAC) [1], these processes have been widely investigated, and hadrons are generally believed to consist of partons —*i.e.* quarks and gluons [2]. In the parton picture, these process is well described by the incoherent scattering of free partons. Therefore, the cross-section of these processes is calculated using the parton distribution functions, fragmentation functions, and cross-section of elementary sub-processes. The "black box" model [3] and the constituent interchange model (CIM) [4] were proposed for calculating the cross-section of the high $P_t$ hadron productions. Both models use empirical forms for cross-sections. Quantum chromodynamics (QCD) developed in recent years [5, 6] raises the possibility of calculating the cross-sections of elementary parton sub-processes. Those cross-sections in the lowest order are listed in Table 1 [7]. The calculated values in the QCD framework agree reasonably with data [8, 9].

* Now at the National Laboratory for High Energy Physics, Ibaraki-ken Japan.

Table 1. The amplitude for the elementary sub-processes of QCD to lowest order.

| Sub-process | $\lvert A\rvert^2$ |
|---|---|
| $q_i\, q_j \to q_i\, q_j$ $\quad i \neq j$<br>$q_i\, \bar{q}_j \to q_i\, \bar{q}_j$ | $\frac{4}{9}\,\frac{s^2+u^2}{t^2}$ |
| $q_i\, q_i \to q_i\, q_i$ | $\frac{4}{9}\left(\frac{s^2+u^2}{t^2}+\frac{t^2+s^2}{s^2}\right)-\frac{8}{27}\,\frac{s^2}{ut}$ |
| $q_i\, \bar{q}_i \to q_j\, \bar{q}_j$ | $\frac{4}{9}\,\frac{t^2+u^2}{s^2}$ |
| $q_i\, \bar{q}_i \to q_i\, \bar{q}_i$ | $\frac{4}{9}\left(\frac{s^2+u^2}{t^2}+\frac{t^2+u^2}{s^2}\right)-\frac{8}{27}\,\frac{u^2}{st}$ |
| $q_i\, \bar{q}_i \to g\ g$ | $\frac{32}{27}\,\frac{u^2+t^2}{u\,t}-\frac{8}{3}\,\frac{u^2+t^2}{s^2}$ |
| $q_i\, g \to q_i\, g$ | $-\frac{4}{9}\,\frac{u^2+s^2}{u\,s}+\frac{u^2+s^2}{t^2}$ |
| $g\ g \to q_i\, \bar{q}_i$ | $\frac{1}{6}\,\frac{u^2+t^2}{u\,t}-\frac{3}{8}\,\frac{u^2+t^2}{s^2}$ |
| $g\ g \to g\ g$ | $\frac{9}{2}\left(3-\frac{u\,t}{s^2}-\frac{u\,s}{t^2}-\frac{s\,t}{u^2}\right)$ |

Note) $q$ and $g$ denote quark and gluon, respectively. $s$, $u$, and $t$ are the Mandelstam variables for the elementary sub-processes. The cross-sections are given by using these amplitudes,

$$\frac{\mathrm{d}\sigma}{\mathrm{d}t}=\pi\alpha_s^2(Q^2)\,\frac{|A|^2}{s}\,.$$

Many of the experiments to study "hard processes" have been performed with nuclear targets because of their ease of handling and their copious yields. Data with the nuclear targets are then extrapolated to estimate the cross-section per nucleon. In addition to the extrapolation, the $A$-dependence itself contains important information on the mechanism of the process. For example, in the "soft" hadronic process (such as the total cross-section), the Glauber theory predicts $A^{2/3}$ dependence. This effect has been confirmed by experiments [10]. On the other hand, for a "hard process" a linear $A$-dependence is expected by the parton model.

The first experimental data on the $A$-dependence of high $P_t$ hadron production were obtained by the Chicago-Princeton group [11]. The $A$-dependence was parametrized as;

$$E\frac{\mathrm{d}\sigma}{\mathrm{d}^3p}(P_t, A) = A^{\alpha(P_t)}\cdot E\frac{\mathrm{d}\sigma}{\mathrm{d}^3p}(P_t, A=1)\,. \tag{1}$$

They found values of $\alpha(P_t)$ significantly greater than 1. Several other experiments have been performed [12–17] and confirmed this "anomalous" $A$-dependence. The results of these experiments in proton-nucleus collision are shown in Fig. 1, and are summarized as following;

1. The $A$-dependence is parametrized by $A^{\alpha}$ reasonably well. However, the number of targets is not enough to distinguish the $A$-dependence from other forms.
2. $\alpha$ is almost independent of energy for all particle types [17].

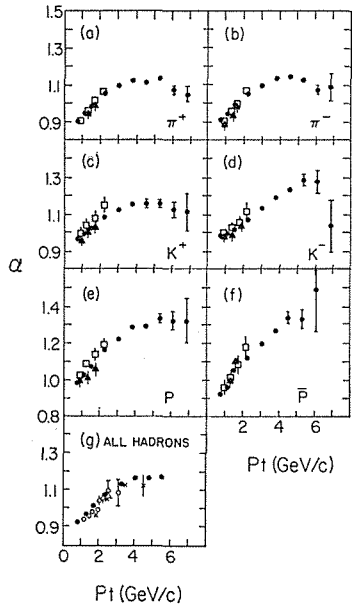


Fig. 1. The $A$-dependence exponent for single hadron production as a function of $P_t$ for proton-nucleus collisions.
The data points are;
closed circle: 400 Gev/c (Ref. 17),
open square: 250 Gev/c (Ref. 12),
closed square: 28.5 Gev/c (Ref. 13),
open circle: 400 Gev/c (Ref. 16),
cross: 400 Gev/c (Ref. 15).

3. For all particle types, $\alpha$ increases with $P_t$ starting from the value less than 1 at $P_t$ around 1 Gev/c and exceeds 1 around $P_t=2$ Gev/c.
4. The dependences of $\alpha$ on $P_t$ of $\pi^+$, $\pi^-$, and $K^+$ are very similar. These $\alpha$'s increase with $P_t$, but have a plateau above 4 Gev/c with the value of 1.13~1.15. Above 6 Gev/c $\alpha$'s show the tendency of decrease, although the statistics is poor. On the other hand, $\alpha$'s for $K^-$ and $\bar{p}$ seem to continue to increase and reach about 1.3 at $P_t$ around 6 Gev/c. The $\alpha$ for protons falls somewhat between that of pions and $\bar{p}$.

Recently, the $A$-dependence for high $P_t$ hadron production has been measured with incident negative pion beam [18]. They found that the behavior of $\alpha$ is very similar to that for proton beam except the $K^-$ production. The $\alpha$ for $K^-$ production seems to have a plateau in contrast to continuous increase in the case of proton beam. But, unfortunately the data for $P_t$ above 4 Gev/c is statistically poor.

There have been many theoretical studies and models relating to the $A$-dependence of high $P_t$ hadron production. These can be classified into the following three groups.

(a) The coherent tube model [19] assumes that the nucleons contained in a tube through which the hadron passes behave collectively just like one single hadron. The effective mass is the total mass of nucleons in the tube. This model gives a linearly rising $\alpha$ with increasing $P_t$.

(b) The multiple scattering model [20–25] postulates that the particle with high $P_t$ is produced by the several "hard" scatterings in the nucleus. This model generally gives the following $A$-dependence;

$$E\frac{d\sigma}{d^3p} = c_1 \cdot A + c_2 \cdot A^{4/3} + c_3 \cdot A^{5/3} + \cdots . \qquad (2)$$

(c) The multi-quark cluster model [26, 27] assumes that there exists $i$-nucleon states ($3i$-quark states) in the nucleus with some probability. The partons in a $3i$-quark state can have momenta up to $i$ times as large as that of single nucleon, and are expected to be a source of the "anomalous" $A$-dependence for the high $P_t$ hadron production.

The $A$-dependence for other "hard processes" has been also studied.

Recently, the European Muon collaboration (EMC) performed an experiment on muon deep inelastic scattering using deuterium and iron targets. They found that the structure function of iron was significantly different from that of deuterium (now called the EMC effect) [28]. The same effect was also seen by a SLAC-MIT-Rochester group by re-analyzing their electron-deuterium and empty target (steel or aluminum) data [29]. This $A$-dependence can not be explained by Fermi motion only [30, 31]. Several explanations have been proposed [32], such as an enhancement of the probability of $\Delta$ in nucleus [33], the multi-quark cluster model [34–36], percolation of colors in the nucleus [37], an enhancement of the pion-sea in nucleus [38], change of the confinement scale [39], the diquark model [40], and an effect of a quark-gluon plasma [41]. Both experimentally and theoretically, the situation is still at an early stage of understanding.

For lepton pair production, a linear $A$-dependence has been observed in a proton-nucleus collision [42]. In pion production of dileptons, a Chicago-Illinois-Princeton group reported an "anomalous" $A$-dependence [43]. However, two experiments performed recently at the CERN SPS show a linear $A$-dependence in a similar kinematic region [44, 45].

An "anomalous" $A$-dependence has been also reported in some mass regions [16] and $P_t$ regions [15], for the di-hadron production in hadron-nucleus collisions.

The present experiment has been performed at the Fermi National Accelerator Laboratory (FNAL). This paper presents only the results on the measurement of the nuclear weight dependence of the single hadron productions at 400 Gev/c, based on the data obtained in the first running period of this experiment. The results on the other subjects of the single hadron productions will be presented elsewhere [46, 47].

## II. APPARATUS

### A. Overview

The purpose of this experiment is to measure high $P_t$ single particles and high mass pairs of all charged particle types —muons, electrons, and hadrons [48]. The detection of electrons and hadrons requires the aperture to be an open geometry, in contrast to previous dimuon experiments which usually had hadron absorbers upstream of the detectors. On the other hand, the cross section falls off very rapidly with the $P_t$ of single particles or with the mass of pairs, and requires a large luminosity. The luminosity is proportional to the beam intensity, target thickness, the acceptance, and running time. The critical one is the beam intensity, because it can be easily increased by order of magnitude (in principle up to the full accele-

rator intensity of $5\times10^{13}$ proton per pulse) in contrast to others. In order to run with a high beam intensity, one has to reduce the background as much as possible, since the single rate in the detector is limited to the order of 1 MHz with the present technology. In our case, the main backgrounds are due to low $P_t$ charged and neutral particles. It is obvious that the requirement of high intensity as well as open geometry is very hard to achieve. In fact, our experiment is the first one to attempt an open geometry and high luminosity experiment at high energies.

With the above requirements, our apparatus was designed as shown schematically in Fig. 2. The design details for high intensity running include the following;

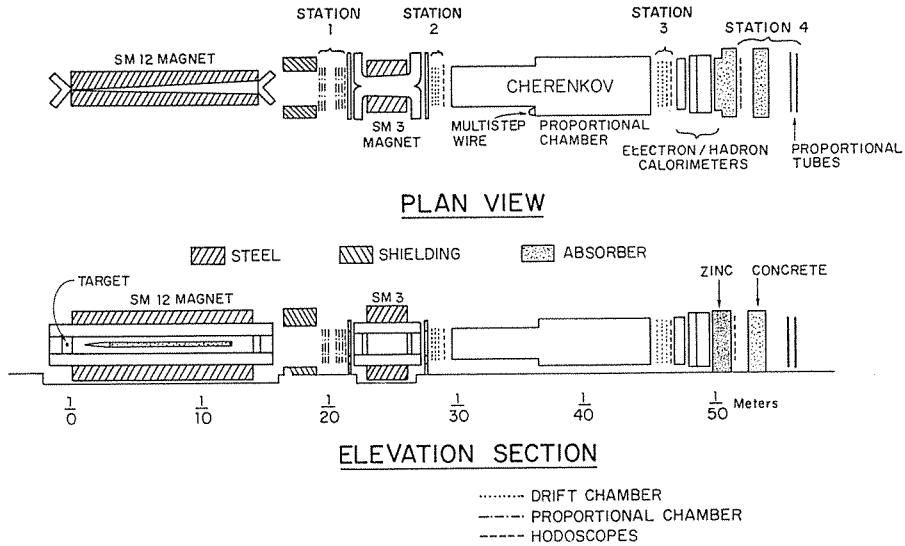


Fig. 2. Schematic view of the apparatus

i) Immediately following the target, a spectrometer magnet with large $P_t$ kick is placed. Thus the spectrometer focuses only high $P_t$ particles in the aperture and sweeps out the low $P_t$ particles which have an intensity several orders of magnitude greater than that of high $P_t$ particles. All the detectors were placed downstream of this magnet.

ii) The neutral particles are well shielded by the beam dump placed inside the magnet and the magnet yoke, and can not hit the detectors directly.
Also, our apparatus has the following features.

iii) A complete particle identification system is provided to make the maximum use of the open geometry. Electrons and hadrons are distinguished by the electromagnetic and hadron calorimeters. The muons are identified by muon detectors placed behind the calorimeter and absorbers. The hadron species (pions, kaons, and protons) are separated by the ring imaging Cherenkov counter placed between the spectrometer and the calorimeter.

iv) The large $P_t$ kick of the magnet together with the open geometry results in an excellent momentum or mass resolution. A mass resolution of order 0.1% is expected.

v) A second analyzing magnet is placed between the first and second detector stations. This magnet provides an independent momentum measurement with moderate resolution (order of 1%). This magnet is also very important for distinguishing the particles produced at the target from those produced at the beam dump or elsewhere.

### B. Beam

Protons slowly extracted from the synchrotron were brought to the Meson target, then diffractive protons produced at this target were transported to our experimental target. The direction of the incident beam had an finite angle with respect to the center line of the apparatus due to the lack of some magnet elements in the beam line in the present experiment. The angle was 3.4 milliradians upward in the vertical direction and 10 milliradians to the left hand side in the horizontal direction. The beam spills were about one second long with a 12 to 15 second interval. The protons in the spill were bunched into R.F. buckets separated by 18.9 ns (nano second$=10^{-9}$ sec). The length of one bucket was less than one ns. These bunches are due to the phase stability of R.F. acceleration in the synchrotron and are not debunched at extraction time. Because of this feature, it was essential to have the time resolution of our detectors compatible with the R.F. bucket resolution.

The position and profile of the beam were monitored by a segmented wire chamber (SWIC) positioned about 75 cm upstream of the target. The intensity of the beam was monitored by a secondary emission monitor (SEM). These monitors were remotely movable and were out of the beam to reduce the background which produced from these monitors during the data taking. These monitors were occasionally put into the beam to calibrate the other monitors between the runs. The beam intensity hitting the target was monitored by the scintillation counter telescope located at 90 degrees in the laboratory system (called the 90 degree monitor). The typical beam intensity during the data taking was $4\times10^{9}$ proton per pulse.

### C. Targets

Three different materials —Be, Cu, and W were used as targets to measure the atomic weight dependence of the cross section. The sizes and other parameters of the targets are listed in Table 2. The targets were made in rectangular plates having a thickness of around 1 mm and a width of 38 mm in the vertical and horizontal direction, respectively. The thickness was chosen as thin as possible to reduce the multiple scattering in the target but comparable with the vertical beam size to not reduce the luminosity. In the horizontal direction, the width was wide enough to contain all the beam. The length was chosen to give approximately the same number of nucleons. The targets were held by the target holder at 2.5 cm intervals in the vertical direction. The holder was placed in a box filled with helium, and remotely moved in both vertical and horizontal directions. The position was displayed by means of a motor drive counter. The horizontal position of the target

was determined by scanning the beam profile by the vertical copper flag (1.1 mm wide) attached on the top of the holder. The fraction of the beam hitting the target was calculated from the results of vertical scans. The SEM was also put in the beam to normalize the counting rate of the 90 degree monitor. Fig. 3 shows a typical result of the horizontal and vertical scans. The typical beam size was 4.5 mm and 1.0 mm FWHM in the horizontal and vertical directions, respectively.

Table 2. Parameters of the targets.

| | Be | Cu | W |
|---|---|---|---|
| Horizontal width (mm) | 38.3 | 38.1 | 38.1 |
| Vertical thickness (mm) | .996 | .914 | 1.059 |
| Length (mm) | 101.8 | 25.8 | 13.1 |
| Nuclear weight $A$ | 9.01 | 63.54 | 183.85 |
| Number of nucleons in unit area ($\times 10^{25}/cm^2$) | 1.13 | 1.39 | 1.52 |
| Density ($g/cm^3$) | 1.848 | 8.96 | 19.3 |

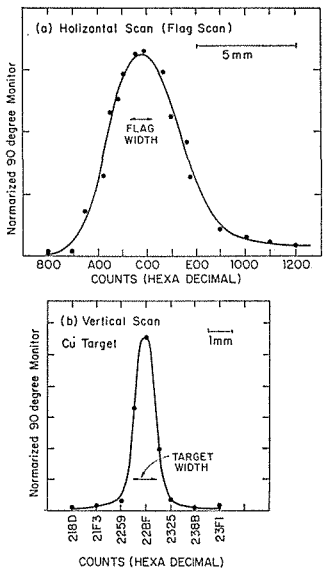


Fig. 3. Beam profile measured by
(a) the copper flag in the horizontal direction,
(b) the Cu target in the vertical direction.

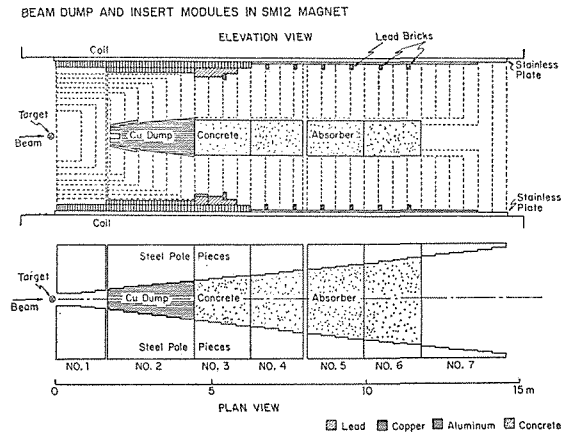


Fig. 4. The beam dump and the pole piece inserts in the SM12 magnet.

## D. Magnets

### SM12

The upstream magnet placed behind the target (about 10 cm downstream) is a conventional dipole magnet called SM12. The detail of the construction is described elsewhere [49]. The steel yoke is 14.4 m long, 2.7 m wide, 5.2 m high, and weighs about 1200 tons. The field aperture is 0.93 m $\times$ 1.3 m in cross section.

The magnetic field was produced in the horizontal direction, thus it bends charged particles vertically.

The coil is made of aluminum conductor to reduce the cost. The cross section of the conductor was 6.15 cm square and has a hole 1.4 cm in diameter for cooling water. The coil consists of 14 layers with 14 turns in each layer, and has 196 turns in total. The top part of the coil is fixed to the return yoke by a stainless steel shelf bridged between pole pieces, and the bottom part sits on the return yoke steel. The part outside the yoke is bent at 45 degrees as shown in Fig. 2.

The maximum current is 4150 amperes with a total power of 1.2 MW and gives about 9 Gev/c $P_t$ kick. For present data taking, the current was set at 2000 amps giving a 5.5 Gev/c $P_t$ kick.

**Beam Dump and Insert Modules**

Since the target is placed close to the magnet and is small in size, the aperture can be small at the upstream part of the SM12 magnet. The tapered pole pieces are inserted in the gap, to produce as high a field as possible. The details of the pole pieces are shown in Fig. 4. These insert pole pieces are divided into 7 modules and the pole faces are tapered so that the gap in the horizontal direction varies from 10 cm to 86.4 cm. The beam dump made of copper is installed inside the second module. The beam dump starts at 1.72 m from the upstream face of the magnet pole and is 2.74 m long. The beam dump is 17.9 cm thick at the upstream face (including the copper plates added. See below.) and 30.5 cm at the end in the vertical direction. Following the copper beam dump, the concrete absorbers are mounted inside of modules no. 3 to no. 6. These absorbers are 28 cm thick in the vertical direction and total 7.32 m in length. The magnet gap was filled with helium to reduce multiple scattering and the conversion of photons.

At the early stages of the experiment, very heavy backgrounds were observed in the detectors. After several studies of the backgrounds, the following two modifications were made to reduce the backgrounds to enable running at higher intensities.

1. 1.9 cm thick copper plates were added on the top and the bottom of the copper beam dump. By adding these copper plates, the backgrounds were reduced considerably at the cost of acceptance in the small angle region.
2. Lead bricks (5 cm high and 10 cm thick along beam) were placed on the top and bottom surfaces of the insert modules. The angle of the lead bricks was carefully chosen so that the photons from the target always hit the upstream face of the bricks and the shower was absorbed in the lead bricks [50].

**SM3**

The second magnet (called SM3) is also a conventional dipole magnet. The magnet is 3.23 m long, and the aperture is 1.68 m high and 1.35 m wide at the upstream face of the magnet. The width of the aperture is tapered and is 1.50 m at the downstream face of the magnet. The coil was also made of aluminum conductor of the same size as that of the SM12 magnet. Flux return iron mittor plates

of 5 cm thick are placed both upstream and downstream of the magnet to protect the phototubes of hodoscopes from leakage magnetic flux. The magnet gives about 0.9 Gev/c $P_t$ kick with a current of 4200 amps. During the present data taking run the current was set at 3282 amps due to the shortage of power for the power supply; the $P_t$ kick was 0.72 Gev/c. A helium bag made of polyethylene was placed in the gap to reduce multiple scattering.

### Field Measurement

The magnetic field of the magnets was measured using the ZIPTRAK system. The ZIPTRAK cart has three coils which measure $x, y, z$ components of the magnetic field. This cart moves along an aluminum guide beam in the beam direction. The field values were recorded at regular intervals in the beam direction. The guide beam can be moved in the horizontal and vertical directions. The movement of the guide beam and cart can be controlled by a computer and the field measurements at the set of grid points can be made automatically. Since ZIPTRAK measures only the relative field from the starting points, the absolute field values were measured by the NMR method at several points. Fig. 5 shows the example of the field variations along the beam line for the horizontal component of the SM12 and SM3 magnets.

## E. Hodoscopes and Chambers

As shown in Fig. 2 our apparatus has 4 stations of detectors —each consisted of one or two hodoscope planes for triggering and several wire chambers for record-

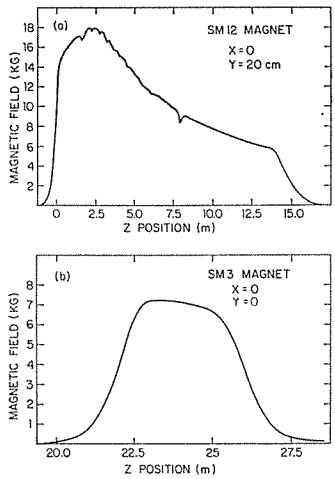


Fig. 5. The major component ($x$-component) of the magnetic field The $x, y$, and $z$ axes are taken in the horizontal, vertical, and the the beam direc tions, respectively.
(a) for SM12 at $X$=0., $Y$=2.0 cm
(b) for SM3 at $X$=0., $Y$=0.

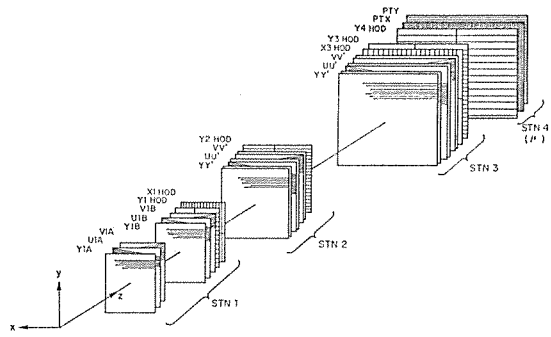


Fig. 6. Schematic view of the hodoscopes and wire chambers. The coordinate system is also indicated.

ing the trajectories of the particles. The fourth station is placed behind the calorimeter and the zinc and concrete hadron absorbers. This station is used for triggering and measuring the trajectories of muons. In Fig. 6, a schematic view of the hodoscopes and wire chambers is shown. Our coordinate system is also shown in the figure. The center line of the apparatus is chosen as the $z$-axis. The $x$-axis and $y$-axis are chosen in the horizontal and vertical directions, respectively.

### Hodoscopes

In Table 3, the specifications of the hodoscopes are listed. The $X$-hodoscopes are segmented into two parts (up and down) in the vertical direction and into 12 or 13 parts in the horizontal direction. The Y-hodoscopes are segmented into left and right in the horizontal direction, and into 12 to 17 parts in the vertical direction. The light from each scintillator is collected in a R329 phototube (Hamamatsu TV Co.) through an adiabatic light guide. NE110 scintillator is used for all counters. Station 1 and 3 have both X and Y hodoscopes, while station 2 and 4 have only Y hodoscopes.

Table 3. Specifications of the hodoscopes

| | Hodoscope plenes | | | | | |
|---|---|---|---|---|---|---|
| | Y1 | X1 | Y2 | X3 | Y3 | Y4 |
| Z location (m) | 21.01 | 21.04 | 28.32 | 46.66 | 46.92 | 51.87 |
| Aperture Hor. (cm) | 121.9 | 121.9 | 162.6 | 264.2 | 264.2 | 294.6 |
| Vert. (cm) | 152.4 | 152.4 | 172.7 | 233.7 | 233.7 | 254.0 |
| Segmentation Hor. × Vert. | 2×12 | 12×2 | 2×17 | 13×2 | 2×13 | 2×14 |
| Counter element | | | | | | |
| Width (cm) | 12.7 | 10.16 | 10.16 | 22.50 (11.03)* | 17.78 (19.05)* | 17.78 (20.32)* |
| Length (cm) | 60.96 | 76.20 | 81.28 | 116.84 | 132.08 | 147.32 |
| Thickness (mm) | 4.76 | 4.76 | 3.715 | 6.35 | 6.35 | 6.35 |

*) counters of both ends

### Chambers

In order to record the trajectories of particles, multi wire proportional chambers (MWPC) were used in station 1 to accept the high counting rate. On the other hand, drift chambers were used for stations 2 and 3 to achieve good space resolution, because lower counting rates were expected at those stations due to the large $P_t$ kick of the SM12 and SM3 magnets. The specifications of the chambers are listed in Table 4.

Station 1 has six MWPC's with three wire directions to allow multi-particle reconstruction. The Y chamber has horizontal wires, while the U and V chambers have wires tilted by an angle of $\theta = \pm\tan^{-1}(1/4)$ with respect to the horizontal direction. Two sets of Y, U, V chambers were placed with a separation of 1.2 m to give a reasonable lever arm for tracking. The wire spacing is 2 mm for the Y

Table 4. Specifications of the chambers

| | | Z (m) | Aperture X (cm) | Y (cm) | Wire space (mm) | Number of wires |
|---|---|---|---|---|---|---|
| Station 1 | Y1A | 18.91 | 128.3 | 149.6 | 2.0 | 736 |
| | U1A | 19.17 | 128.3 | 152.4 | 1.94 | 896 |
| (MWPC) | V1A | 19.42 | 128.3 | 152.4 | 1.94 | 896 |
| | Y1B | 20.11 | 128.3 | 149.6 | 2.0 | 736 |
| | U1B | 20.36 | 128.3 | 152.4 | 1.94 | 896 |
| | V1B | 20.62 | 128.3 | 152.4 | 1.96 | 896 |
| Station 2 | YY′ | 27.55 | 167.6 | 178.8 | 10.0 | 176 |
| (DC) | UU′ | 27.80 | 167.6 | 182.9 | 9.7 | 208 |
| | VV′ | 28.06 | 167.6 | 182.9 | 9.7 | 208 |
| Station 3 | YY′ | 45.79 | 269.2 | 233.3 | 20.0 | 112 |
| (DC) | UU′ | 46.04 | 269.2 | 242.6 | 19.4 | 144 |
| | VV′ | 46.30 | 269.2 | 242.6 | 19.4 | 144 |
| Station 4 | PTX | 54.81 | 365.8 | 315.0 | 25.4 | 144 |
| (Prop. Tube) | PTY | 55.85 | 363.2 | 375.9 | 25.4 | 142 |

chamber, and 1.94 mm for the U and V chambers. We used an Argon/$CO_2$ (17%)/ Freon(.3%) gas mixture for the station 1 MWPC's.

The chambers is stations 2 and 3 consist of six planes of drift chambers with the same three wire directions as those of the station 1. The two planes with the same wire direction were constructed in one chamber frame and staggered by a half wire spacing to resolve the so-called left-right ambiguity. The spacing of the sense wires in the Y (U and V) chambers is 10 mm (9.7 mm) and 20 mm (19.4 mm) for stations 2 and 3, respectively. 50% Argon and 50% ethane gas was circulated into the chambers through ethyl alcohol at a temperature of 0°C. The offset of the TDC time zero and the space-time relation were determined by off-line analysis. The space-time relation of station 2 chambers had a good linearity, while that of station 3 required a form quadratic in time. The reason is that the station 3 chambers have longer drift length and have a weak electric field region. After correcting the propagation delay of signals along the wires (velocity of 0.8 times light velocity), a spatial resolution of around 200 microns was obtained for both stations.

**Proportional Tubes**

Two planes of proportional tubes with the wires in the horizontal and vertical direction are placed at station 4. Each plane was made of 18 units of the extruded aluminum tube. One unit of extruded tube contains 2 layers of 8 cells with cell size of $2.5 \times 2.5$ cm. Those two layers are staggered by a half cell to avoid the dead regions due to the wall between the cells. The sense wires of staggered cells are connected together. The same gas mixture as the station 2 and 3 drift chambers was used for the proportional tubes.

## F. Calorimeter

The calorimeter is placed behind the station 3. The roles of the calorimeter are;

1. to give the fast electron and hadron trigger signals (The details will be described in Sec. III-A)
2. to identify muons, electrons, and hadrons in the off-line analysis.

### Construction

The calorimeter consists of two parts —the electromagnetic part (EM part) and the hadron part (H part) as shown in Fig. 7. Both are ordinary sampling type calorimeters which consist of plastic scintillators and absorbers of dense material. The construction parameters are listed in Table 5. Because of the large

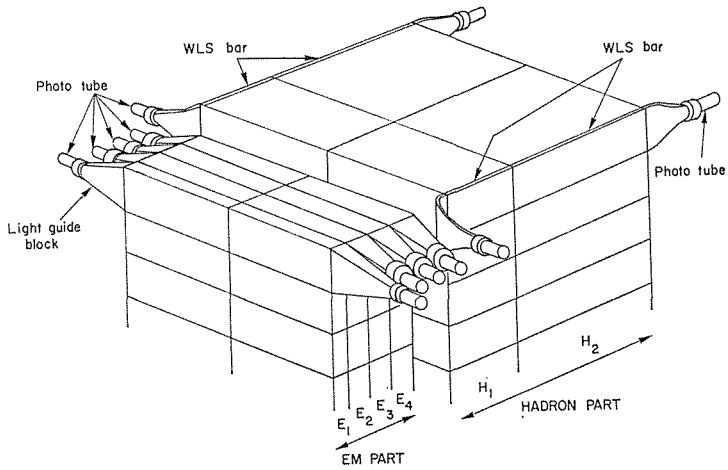


Fig. 7. Schematic view of the calorimeter.

Table 5. Specifications of the calorimeter

| | Modules | | | | | |
|---|---|---|---|---|---|---|
| | E1 | E2 | E3 | E4 | H1 | H2 |
| Absorber | Pb (3 mm) | | | | Fe (25 mm) | Fe (50 mm) |
| Scintillator | Kyowa SCAS1101 (20 cm × 148 cm × 6 mm) | | | | Kyowa SCAS1101 (20 cm × 155 cm × 6 mm) | |
| Light collection | Acrylic block | | | | WLS (Altulor 1290) + twisted light guide | |
| Photo tube | R1565 3″$\phi$, 6 st. | R1476 (Hamamatsu TV) 5″$\phi$, 6 stage | | | R1565 (Hamamatsu TV) 3″$\phi$, 6 stages | |
| Number of layers | 4 | 9 | 9 | 10 | 12 | 20 |
| Radiation length | 2.41 | 5.43 | 5.43 | 6.03 | 17.53 | 58.58 |
| Integral* | | | | 21.58 | 39.11 | 97.19 |
| Absorption length | 0.13 | 0.28 | 0.28 | 0.31 | 1.90 | 6.13 |
| Integral* | | | | 1.08 | 2.98 | 9.11 |

*) Including X3 and Y3 hodoscopes and Pb sheet (12 mm, 2.27 r.l.) in front of the calorimeter

volume of scintillator, a new plastic scintillator developed by Kyowa Gas Co. with relatively low cost and high performance (Kyowa SCAS1101) was chosen for both parts (see Appendix I).

The EM part consists of 32 layers of 3 mm lead and 6 mm scintillators totaling 19 radiation lengths. The scintillators are grouped into 4 modules (4, 9, 9, and 10 layers from upstream) in the longitudinal direction. A 1.27 cm thick lead sheet was placed in front of the calorimeter. This lead sheet and the thin first module (about 2 radiation lengths) was designed to provide good electron hadron separation based on our test results [51] using a small prototype calorimeter. The aperture is 2.8 m and 2.4 m in the horizontal and vertical directions, respectively. Each module is divided into $2 \times 12$ segments in the same way as the Y-hodoscopes. The light output of each segment is collected onto a 6-stage phototube through a acrylic light guide. 3″ diameter tubes (Hamamatsu TV Co. R1565) are used for the first thin modules (4 layers). The rest of modules use 5″ diameter phototubes (Hamamatsu R1476). The 6-stage tubes were chosen with the following reasons:

1. The expected signals were large enough so that a large amplification was not necessary. A typical amplification of $2 \times 10^4$ for 5″ tubes and $10^5$ for 3″ tubes was required in contrast to that of $10^6$ for 12-stage tubes.
2. Good linearity can be achieved over a wider range than with higher stage tubes.

The hadron part consists of two modules in the longitudinal direction. The first module consists of 12 layers of 2.5 cm thick iron and 6 mm thick scintillators. The second module consists of 20 layers of 5 cm thick iron and 6 mm thick scintillators. The total thickness amounts to 9 absorption lengths including the EM part (about 1 absorption length). The aperture is 3 m and 2.6 m in the horizontal and vertical directions. These two modules are divided into $2 \times 13$ segments in the same way as the EM part. The light output of each segment was collected on a wave length shifter bar (ALTUROR 1922) then led to a 3″ diameter phototube (R1565) through an acrylic light guide. The attenuation of the light along the wave shifter bar is corrected by masking the surface of the wave shifter bar with aluminized mylar sheet. The masked area decreases from phototube end to far end so that the light collection to the phototube does not depend on the position of the wave shifter bar. The whole calorimeter was covered by a vinyl hut with an air conditioner to keep the temperature constant.

The signals from the dynodes of all the phototubes of the calorimeter were summed up with an array of linear adders. The sum was used for the fast triggers. The signal from each phototube anode was fed into a fast ADC circuit having a conversion time of 2 micro second. This fast ADC has a quadratic response and was developed at Nevis Labs. The signals from the X3 and Y3 hodoscopes were also fed into the ADC's to provide additional information on particle identification.

**Calibration and Performance**

The pedestals and the quadratic response of each fast ADC was periodically calibrated. These parameters were written on magnetic tapes at the beginning of

each run and used in the off-line analysis.

The gain of each phototube was set roughly equal to each other by adjusting the high voltage using the minimum ionization signal of muons. In the off-line analysis, the gain was precisely evaluated from data by the following procedure. The energy deposit of the $i$-th particle in the calorimeter, $E(i)$, is given by;

$$E(i) = \sum_j \frac{a_j \cdot Q_j(i)}{F_{\mathrm{corr}}(x)} \tag{3}$$

where $a_j$ is the gain of $j$-th phototube to be evaluated and $Q_j(i)$ is the output charge of $j$-th phototube for the $i$-th particle. $F_{\mathrm{corr}}(x)$ is the factor due to the attenuation of light through scintillator. This factor is known from test measurements and is normalized to 1 at the far end of the scintillator from the phototube. The hit position of the particle ($x$) is known from the chamber data. The summation in $j$ includes the appropriate number of segments around the track to reduce the effect of noise. Then the $a_j$'s were determined so as to minimize the following quantity,

$$\chi^2 = \sum_i \left[\frac{E_{\mathrm{in}} - E(i)}{\sqrt{E_{\mathrm{in}}(i)}}\right]^2 \tag{4}$$

where $E_{\mathrm{in}}(i)$ is the energy of the $i$-th particle determined precisely by the track reconstruction through the spectrometer. The errors of the $a_j$'s were estimated to be around 3%. The energy response and energy resolution of the calorimeter for hadrons are shown in Fig. 8 and 9, respectively. The energy resolution can be represented by

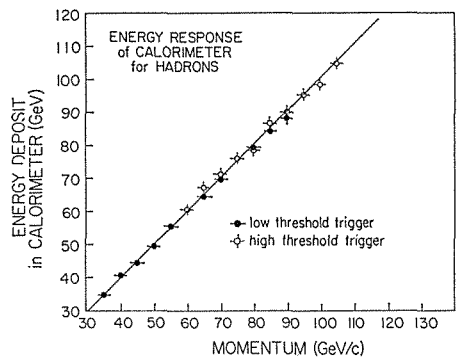


Fig. 8. Energy response of the calorimeter for hadrons The line is drawn for guiding eyes only.
The data points are;
open circle: high threshold triggers,
closed circle: low threshold triggers.

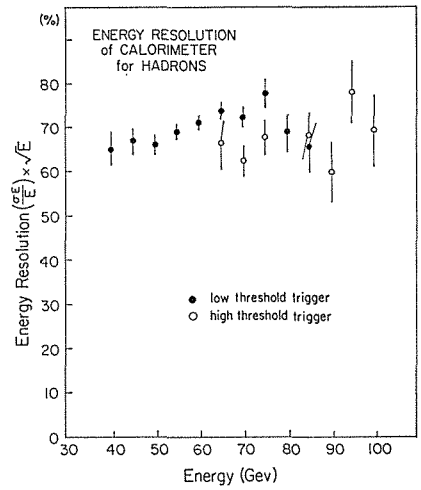


Fig. 9. Energy resolution of the calorimeter versus energy for hadrons.
The data points are;
open circle: high threshold triggers,
closed circle: low threshold triggers.

$$\frac{\sigma_E}{E} \simeq \frac{0.75}{\sqrt{E(\text{Gev/c})}}, \tag{5}$$

This value is compatible with other calorimeters with similar configurations [52].

### G. Ring Imaging Cherenkov Counter

The hadron species are identified by use of a ring imaging Cherenkov counter located between station 2 and station 3. The details of the Cherenkov counter are described elsewhere [47, 53]. The counter consists of a vessel which contains the radiator gas, mirrors, and a photon detector. The vessel, 15.2 m long and large enough to cover the aperture (3.1 m×2.8 m), is made of thin aluminum. Helium is used as the radiator gas and is circulated through a purifier to maintain the high purity. The gas was kept at room temperature and at slightly above atmospheric pressure. The threshold momenta for Cherenkov emission are 16 Gev/c, 58 Gev/c, and 110 Gev/c for pions, kaons, and protons, respectively.

16 spherical mirrors with focal length of 8 m had been designed to be installed in a 4×4 array. However, in the present experiment only the half of the mirrors were assembled covering the central half of the horizontal aperture.

The multi-step proportional chambers [54] detect the Cherenkov photons. These photon detectors were designed to be mounted on both side of the vessel, but only one of them was available in the present experiment. The active area of the chamber is 40 cm×80 cm. The window of $CaF_2$ crystals separates helium gas and chamber gas, He (97%)/TEA (tetraethylamine, 3%) mixture. The signals are read out from the anode wire plane and both sides of the cathode wire planes. The cathode wires have angles of ±45 degrees with respect to the anode wires to make multi-photon reconstruction possible. The wire spacings are 2 mm for anode and 1 mm for cathode wires. The signals from the chamber are fed into LeCroy 2280 12 bit CAMAC ADC system to record their charge.

The position of the Cherenkov photons was determined by requiring the wires of all three planes to fire. By examining the relation between the total charge on each wire, ghost photons are clearly rejected. The hadron species are determined by examining the distance between the positions of the Cherenkov photons and the ring centers calculated from the trajectories of particles. The resolution of the radius is 2.3 mm in FWHM and the clear $\pi/K/p$ separation is obtained up to 200 Gev/c. The distribution of the number of photons for pions was fit quite well by a Poisson distribution. The average number of photons was found to be 2.7.

## III. DATA ACQUISITION

### A. Triggers

#### Hodoscopes and Trigger Matrices

The logic diagram of the fast trigger system for the hodoscopes is shown in Fig. 10 (a). The signals from hodoscope counters are fed into the 16 channel discriminator (LeCroy 4416), then the ECL output signals are fed into the pulse stretch-

er. In the pulse stretcher, the signals are gated by pulses synchronized to the accelerator R.F. signal. The timing of each counter is carefully adjusted so that the timing of the output pulses from the stretcher are always determined by the accelerator R.F. even though the counter signals have some time jitter due to propagation time difference in the scintillators and phototubes. The outputs of the pulse stretchers are used for all coincidences in the fast logic. This technique makes it possible to achieve one R.F. bucket time resolution even if the counter signals have fairly large time jitter as illustrated in Fig. 11. The outputs of the pulse stretcher are also fed into gated latches (called coincidence registers). The other output

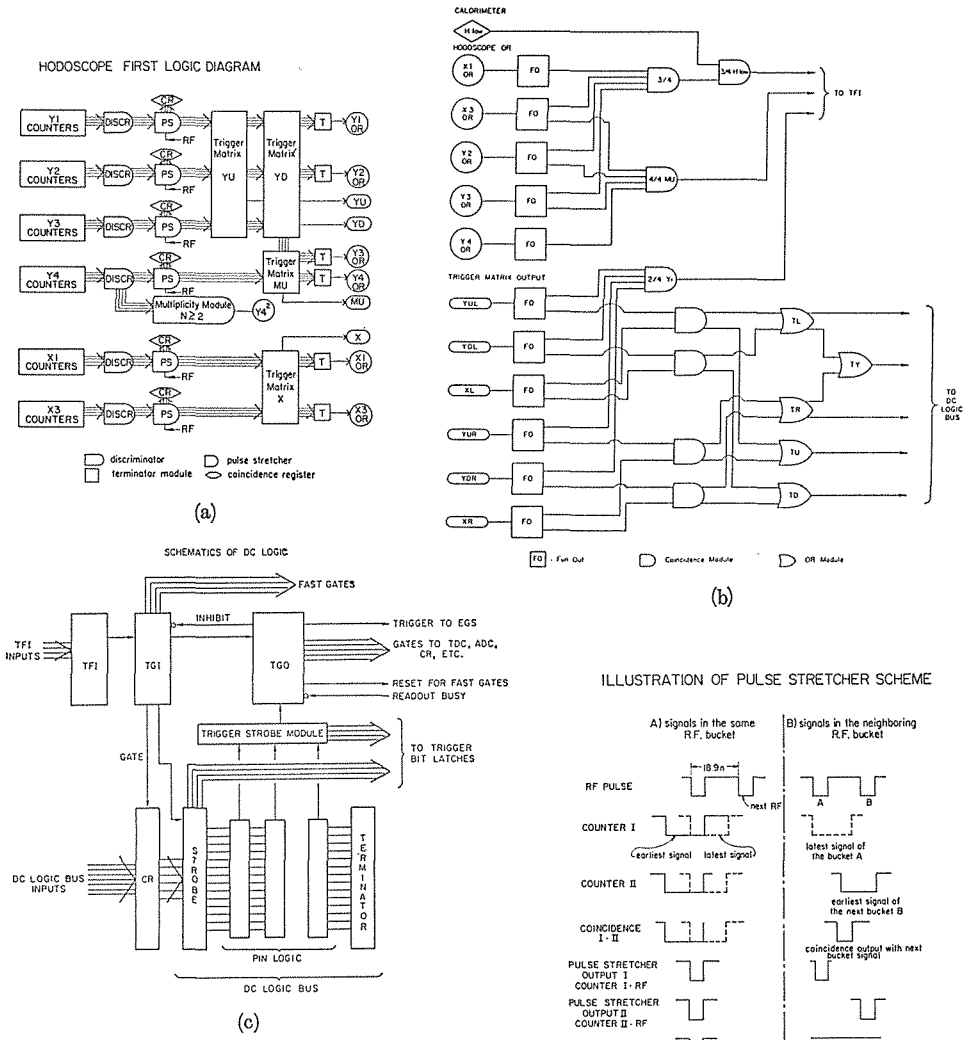


Fig. 10. Logic diagram of the trigger system.
(a) the hodoscope and the trigger matrices,
(b) the fast trigger logic,
(c) the DC logic.

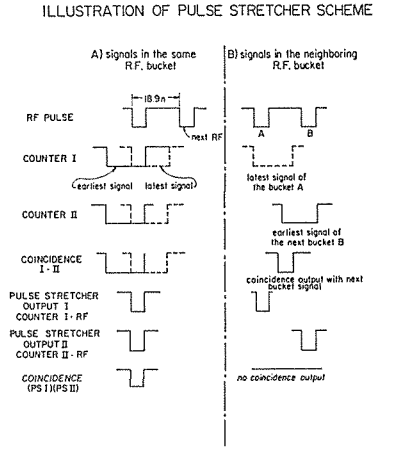


Fig. 11. Timing of the pulses in the pulse stretcher.

signals are fed into the trigger matrix modules through flat cables, and finally ORed in the terminator module.

The trigger matrix produces an output pulse when the configuration of input pulses from the hodoscope counters coincide with a hit pattern stored in the RAM (random access memory) beforehand. The hit pattern is prepared so that trigger signals are produced only for particle trajectories in the acceptance. Three kinds of matrices for the hit pattern were used.

i) Y-matrix; 3 fold coincidence of the Y1, Y2, and Y3 hodoscopes with two sets of pattern. The first pattern is provided for positive particles coming through aperture of the SM12 magnet above the beam dump (called YU). The second one corresponds to those below the beam dump (called YD) for negative particles.

ii) X-matrix; 2 fold coincidence of the X1 and X3 hodoscopes with a pattern corresponding to a particle coming in a straight line from the target.

iii) Mu-matrix; 2 fold coincidence of the Y3 and Y4 hodoscopes.

Table 6. Summary of the fast trigger system

| TRIGGER MATRIX; | logic | output | comments |
|---|---|---|---|
| Y-matrix | Y1·Y2·Y3 | YUL | track above beam dump (left) |
| | | YUR | track above beam dump (right) |
| | | YDL | track below beam dump (left) |
| | | YDR | track below beam dump (right) |
| X-matrix | X1·X3 | XL | track of left hand side |
| | | XR | track of right hand side |
| | | CXL | track hit the Cherenkov mirror on left side |
| | | CXR | track hit the Cherenkov mirror on right side |
| Mu-matrix | Y3·Y4 | MUL | muon track on left side |
| | | MUR | muon track on right side |
| TRACK TRIGGER; | logic | output | comments |
| | (YUL+YDL)·XL | TL | left track (both charges) |
| | (YUR+YDR)·XR | TR | right track (both charges) |
| | (YUL·XL)+(YUR·XR) | TU | positive charged track |
| | (YDL·XL)+(YDR·XR) | TD | negative charged track |
| | TL+TR | TY | any track |
| HODOSCOPE OR; | logic | output | comments |
| | X3L·Y2L·Y3L·Y4L | 4/4MUL | |
| | X3R·Y2R·Y2R·Y4R | 4/4MUR | |
| | X1L, Y2L, X3L, Y3L | 3/4L | any 3 out of 4 planes |
| | X1R, Y2R, X3R, Y3R | 3/4R | any 3 out of 4 planes |
| | Y4L, Y4R | $Y4^2$ | any 2 on Y4 |

It should be noted that these triggering patterns are compared to the hodoscope pattern on the left hand side and on the right hand side independently. The coincidence outputs of these matrices are summarized in Table 6.

Then, the coincidence outputs TL, TR, TU, TD, and TY were provided from the outputs of the trigger matrices mentioned above (called Track signals). L and R denote the left and right sides of the apparatus, respectively.

Among the ORed signals from the terminator modules, the coincidence outputs 4/4MUL(R) and 3/4L(R) were produced. Also $Y4^2$ is produced using a multiplicity module by requiring any 2 hits on the Y4 hodoscope.

The logic of these coincidence outputs are also listed in Table 6. The logic diagram of these triggers is shown in Fig. 10 (b).

**Calorimeter fast triggers**

The signals from the segments of the calorimeter were first summed within the same longitudinal module using linear fan-in circuits. Then the signals from these modules were summed with appropriate weights using attenuators to give the correct energy sum. Two kinds of summed signals were provided;

EL or ER =Sum of the left or right hand side of the EM part (E1+E2+E3+E4).

HL or HR=Sum of the left or right hand side of the EM part (E1+E2+E3+E4) plus the sum of the Hadron part (H1+H2).

The signal EL (or ER) is used to trigger the electron events, while the signal HL (or HR) is used for the hadron events. These signals are fed into risetime-compensated discriminators (LeCroy Models 825) to reduce the time jitter due to the pulse height variation. Threshold levels can be adjusted by attenuators depending on the requirements of the experiment. The set of threshold levels used are listed in Table 7. The output pulses from these discriminators are fed into the DC logic system.

Table 7. Calorimeter fast logic triggers

| Name | Sum | Attenuator (dB) | Discriminator level (mV) | Threshold Energy* 10%~90% (Gev) | Comments |
|---|---|---|---|---|---|
| ELhi | EL | 10 | 15 | — | Electron Trigger |
| ERhi | ER | 10 | 15 | — | |
| Ehi | ELhi or ERhi | | | | |
| HLlow | HL | 0 | 30 | 30~ 52 | Low threshold hadron trigger for TFI and prescaled trog. |
| HRlow | HR | 0 | 30 | 30~ 52 | |
| Hhi | HL+HR | 6 | 30 | 60~105 | High threshold hadron trigger |
| HLche | HL | 6 | 30 | 60~105 | Cherenkov hadron trigger |
| HRche | HR | 4 | 30 | 48~ 84 | |

*) The typical values at the middle of the scintillators are shown.

### DC Logic

The readout system can be triggered by various logic requirements. As shown in Fig. 10 (b), the following combinations of pulses from the hodoscopes, trigger matrices, and calorimeters are fed into a fan-in circuit (called TFI);

3/4L·HLlow,
3/4R·HRlow,
4/4MUL,
4/4MUR,
2/4Ymat,

where 2/4Ymat implies at least two out of 4 Y-matrices (YDR, YDL, YUR, YUL) fired. The TFI output pulses are used to gate the DC logic system to make the final trigger decision for the readout system, as is shown in Fig. 10 (c). The DC logic is a flexible general purpose triggering system developed at Nevis Labs. The fast trigger signals described previously are fed into the DC logic bus. When the DC logic accepts the gate from the TFI, the DC logic interrogates the pattern of trigger signals. When the fast trigger pulses satisfy at least one of the following combinations, the DC logic produces an output pulse (called TGO pulse);

| | | | |
|---|---|---|---|
| i) | Dimuon trigger | (a) | TL·TR·MUL·MUR |
| | | (b) | TU·TD·MUL·XL·$Y4^2$ |
| | | (c) | TU·TD·MUR·XR·$Y4^2$ |
| ii) | Electron trigger | | TY·Ehi |
| iii) | Hadron trigger | (a) | TY·Hhi |
| | | (b) | TL·CXL·HLche |
| | | (c) | TR·CXR·HRche |

The combination i)–(a) is for left-right muon pairs regardless of the muon charges, while i)–(b) and (c) are for opposite sign dimuons. The iii)–(b) and (c) combinations are special combinations used to record information from the ring imaging Cherenkov counter. Di-electron and di-hadron events are included in the electron trigger ii) and hadron trigger iii). The DC logic also produces a TGO pulse for the following prescaled fast trigger patterns;

| | | | |
|---|---|---|---|
| iv) | prescaled triggers | (a) | 4/4MUL (every 1024 counts), |
| | | (b) | 4/4MUR (every 256 counts), |
| | | (c) | 3/4L·HLlow (every 128 counts), |
| | | (d) | 3/4R·HRlow (every 32 counts). |

Events with triggers (a) and (b) monitor the rate of single muons. Events with triggers (c) and (d) are used to determine the efficiency of the calorimeter in the hadron trigger. These events are also used to measure the efficiency of the hodoscopes. Only the events with a hadron trigger and the prescaled triggers (c) and (d) are used in the present analysis.

## B. Readout System

### Data Transport System

Our readout system uses the Nevis data transport system. This system is a

flexible and high speed data acquisition system able to handle 16 bit words at more than 5 MHz. Details of the system are described elsewhere [46, 55]. The schematic of our system is shown in Fig. 12. Subsystems, such as the ADC's, TDC's etc., are connected to the transport bus by transport system modules. The transport bus is a 60 conductor ribbon cable (30 are used, the others are grounded). The transport bus contains 16 data bits, 8 name bits, and 6 control bits. A transport crate has 21 slots. Two slots at each end of the crate are used for bus terminator modules and the remaining 19 slots can be used for transport system modules. Transport system modules are classified into two types —the first are called sources (S) which send the data onto the transport bus, and the second are called destinations (D) which receive the data from the transport bus. They are listed in Table 8. A control word from the PDP-11/45 computer can be sent to the transport bus by an S3 module to initialize the system etc. When the EGS (event generator source) module receives a trigger signal from the DC logic, the EGS module sends

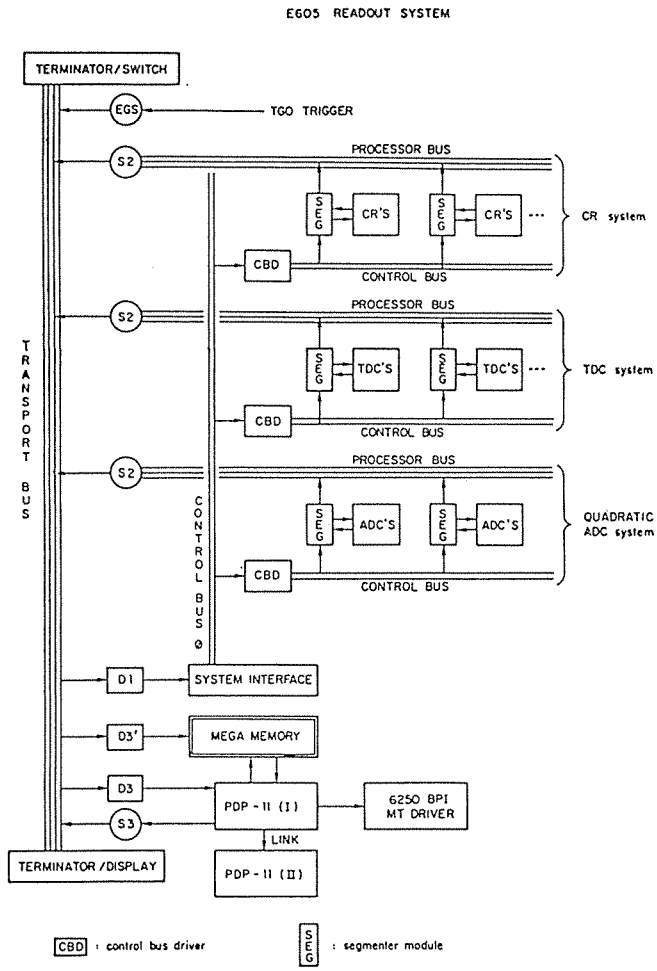


Fig. 12. Schematics of the E605 readout system.

Table 8. Transport system modules

| Module | Function |
|---|---|
| Terminator/Switch | Terminates the transport bus on one end. Allow assertion of data on the bus manually by the switches on front pannel |
| Terminator/Display | Terminates the transport bus on the other end. Displays the status of the bus |
| Event Generator Source (EGS) | Accepts the trigger output from DC logic and asserts a read command to S2 |
| Source 2 (S2) | Sends the data onto the transport bus synchroneously from the sub-system such as ADC's and TDC's |
| Source 3 (S3) | Sends the data or commands asynchroneously to any module through the transport bus from an external device |
| Destination 1 (D1) | Receives the commands asynchroneously from an external device through the transport bus |
| Destination 3 (D3) | Receives the data asynchroneously from an any external device through the transport bus |
| Destination 3′ (D3′) | Modified D3 module for special purpous. Receives the data from S2 through the transport bus and send them to the Mega-memory |

a command to the S2 modules to start the readout of the data. The S2 modules accept detector data from a processor bus and sends data onto the transport bus. The various types of data from the different detectors —ADC's for the calorimeter, TDC's for the drift chambers, coincidence registers (CR's) for the MWPC, hodoscopes, and proportional tubes— are controlled by modules called segmenters. The segmenters send the data from the ADC etc. via a processor bus which is a 50 conductor ribbon cable (half of them were grounded). The processor bus contains 24 bits; i.e. 16 data bits, 4 name bits, and 4 control bits. This bus is designed for extremely fast data transfer (up to 40 MHz).

A control word for the transport bus is received by the system interface through a D1 module and is rebroadcast on the control bus. The control bus is a small slow bus of 34 conductor ribbon cable with 17 bits of data; i.e. 8 address bits and 9 control bits. A control word on the control bus is sent to the segmenters by the control bus driver. The data from the detector on the transport bus is sent by the D3′ module (modified from the standard D3 module) to the Mega-memory. The Megamemory is a fast buffer with 1 megabite of memory built at the University of Washington.

Since the Cherenkov counter data are read through a CAMAC ADC system which is considerably slower than the Nevis transport system, special treatment is needed. As described before, the Cherenkov events have separate triggers and data in the ADC modules are read into the PDP-11 memory through the DR-11 interface only for events with Cherenkov triggers. These data are then sent on the transport bus and transferred to the Mega-memory after the other data from the event are read in.

**On-line system**

Two PDP-11/45 computers are used for our on-line system. The first one (PDP-I) is used for the data acquisition and first level monitoring. The second

one (PDP-II) is used for more sophisticated on-line analysis and monitoring. During the beam spill, the data read by the readout system are accumulated in the Mega-memory, then between the beam spills the data in the Mega-memory are written onto a 6250 bpi magnetic tape. This allows us to store up to 1000 events with 500 words during one beam spill. The PDP-I also accumulates the hodoscope hits, chamber hits, records multiplicities, integrates the scaler data, and displays event pictures or histograms. At the end of a run the counts in the scalers and all histograms can be printed on a printer. PDP-II is linked to the PDP-I; data from the Mega-memory can be transferred to PDP-II. A MULTI program, a flexible general purpose data handling program developed at FNAL, was modified to handle our linked computer system and was used for the PDP-II analysis program.

### C. Data Taking

The target was switched at intervals of a few data tapes so that data taking conditions were similar for different targets. The averaged counting rate for various levels of the trigger are listed in Table 9. The counting rates were almost constant for all targets (within a factor of two). The singles rates at a beam intensity of

Table 9. Average counting rates per spill

| | Be | Cu | W |
|---|---|---|---|
| Intensity (protons on target) | $4.3\times10^{3}$ | $4.3\times10^{9}$ | $4.2\times10^{9}$ |
| 90 degree monitor | 283 | 712 | 1061 |
| Single rates | | | |
| Station 1 hodoscope | $1.5\times10^{7}$ | $1.3\times10^{7}$ | $1.2\times10^{7}$ |
| Station 2 hodoscope | $8.6\times10^{6}$ | $7.0\times10^{6}$ | $6.4\times10^{6}$ |
| Station 3 hodoscope | $1.4\times10^{7}$ | $1.2\times10^{7}$ | $1.1\times10^{7}$ |
| Station 4 hodoscope | $3.8\times10^{4}$ | $2.9\times10^{4}$ | $3.1\times10^{4}$ |
| Fast triggers | | | |
| YU(L+R) | $2.4\times10^{5}$ | $1.5\times10^{5}$ | $1.3\times10^{5}$ |
| YD(L+R) | $2.1\times10^{5}$ | $1.3\times10^{5}$ | $1.1\times10^{5}$ |
| 3/4(L+R) | $5.7\times10^{6}$ | $4.1\times10^{6}$ | $3.6\times10^{6}$ |
| TFI inputs | | | |
| 3/4·Hlow (L+R) | 866 | 1150 | 1480 |
| 4/4MU (L+R) | $1.5\times10^{4}$ | $1.0\times10^{4}$ | $1.2\times10^{4}$ |
| 2/4 Ymat | $4.6\times10^{4}$ | $2.7\times10^{4}$ | $2.2\times10^{4}$ |
| DC logic triggers | | | |
| Total | 157 | 151 | 145 |
| TY·Hhi | 26 | 35 | 43 |
| Cherenkov | 7.43 | 9.39 | 11.25 |
| 3/4·Hlow (prescaled) | 8.24 | 11.2 | 13.4 |
| Live time | | | |
| DC logic | .996 | .997 | .997 |
| Readout system | .840 | .821 | .747 |

Table 10. Total number of events.

| | Targets | | |
|---|---|---|---|
| | Be | Cu | W |
| Total number of protons | $2.9\times10^{13}$ | $3.0\times10^{13}$ | $2.3\times10^{13}$ |
| Total hours | 27 | 26 | 24.3 |
| Data on tape | | | |
| Total | $1.0\times10^{6}$ | $9.7\times10^{5}$ | $1.2\times10^{6}$ |
| TY·Hhi trigger | $1.6\times10^{5}$ | $2.3\times10^{5}$ | $2.4\times10^{5}$ |
| Cherenkov trigger | $4.7\times10^{4}$ | $6.0\times10^{4}$ | $6.7\times10^{4}$ |

$4\times10^{9}$ proton per spill reached the order of 10 MHz on a hodoscope plane and a few MHz for each counter in stations 1 to 3. In order to keep the accidental background reasonable, the beam intensity has been kept below $4\times10^{9}$ proton per pulse. The dead time of the readout system was mainly due to the Cherenkov trigger system which included the slow ADC's as mentioned in Sec. III-B. The hadron trigger rates were about one third of the total trigger rates and the rest of the triggers were mostly di-muon triggers. The total number of events recorded is listed in Table 10. Several special runs were performed for the calibration and study of our detectors, such as runs with no magnetic field in the SM3 magnet (SM3 off), target out runs, etc.

## IV. DATA ANALYSIS

### A. Data Reduction

The raw data were recorded on about 30 rolls of 6250 bpi tape and they were processed with the following procedure. From the sampling analysis, it was found that a large fraction of the recorded events contained real tracks in the aperture, however the most of the di-muon trigger events contained only a single muon track with extra accidental hits. Therefore, in the first step, the events were processed by a track finding program and copied onto a second tape adding the track information to make the first compressed data. At this step only di-muon trigger events which had at least 2 hits in both proportional tube planes in station 4 were processed.

These events were then sorted according to the trigger type of the events. The TY·Hhi trigger events for each target were written on two tapes, while the Cherenkov trigger events for each target were written on one tape.

The third step was to correlate the information from all the detectors such as the energy deposit in the calorimeter, the hits in station 4, the Cherenkov particle identification, etc, then to write only the reconstructed information on the tape. Also in this step, the tracks were traced back to the target and tested whether they satisfied the trigger matrix or not. All such information was also written on the tape. Finally the data were condensed on one tape for the TY·Hhi trigger events for each target. The Cherenkov data for each target were stored in one file on disk. Thus the raw data were compressed onto three tapes without any cuts for

hadron trigger events. As will be seen in Sec. IV-C, about 60% of the hadron trigger events passed all the cuts, thus cuts in the early stage were not necessary.

Using the data from this stage, the final analysis was performed as described in the Sec. IV C to F.

## B. Track Reconstruction

### Track Finding

Three independent tracking programs (called TRACKERS) were developed and cross-checked by comparing the results. These tracking programs used different algorithms and gave essentially the same results for most of the events. These algorithms are described briefly:

TRACKER 1; First, this program finds track segments having 4 or more hits in the 6 chambers of station 1 using a loose aperture cut. Then the program searches the triplet hit clusters of the Y, U and V chambers in stations 2 and 3. In this search, the triplet hits are required to line up with the station 1 segments in the non-bending horizontal plane. The program requires at least 12 chamber hits among the 18 chambers and at least 3 hits in each of the stations 2 and 3.

TRACKER 2; This program starts by listing the triplet hits in the Y, U and V chambers in stations 2 and 3. Then good tracks are selected by testing combinations of the triplet hits of stations 2 and station 3. Then the program searches for hits in station 1 aligned with these candidate tracks in stations 2 and 3. The program requires at least 4 hits in stations 2 and 3, and 3 hits in station 1.

TRACKER 3; The first step of TRACKER 3 is the same as that of TRACKER 1 (but the programs were written independently). Then the program searches the hits in stations 2 and 3, and examines whether they are consistent or not with the segments in station 1. This step starts at one of the Y, U and V views, then repeats in the other views. The hit requirements of this program are almost the same as TRACKER 1.

The tracks thus found by these programs were fitted with straight lines joined at the effective bend plane of the SM3 magnet. The confidence levels of the fit were also calculated.

In the first stage of the data reduction, the TRACKER 1 program was used, since this program had the fastest execution time among the three programs.

### Momentum Reconstruction

At first, the momentum of a particle was calculated from the bend angle in the SM3 magnet obtained by the fit of the tracking program (called 'SM3 momentum'). The $P_t$ kick of the SM3 magnet is parametrized as a function of the $x$ and $y$ coordinates. The function is expanded into symmetric harmonic polynomials as following;

$$H_N(x, y) = Re\{\sum_{n=1}^{N} a_n \cdot (x-iy)^n\} \tag{6}$$

This is the general solution of the two dimensional Poisson equation [56]. $N=4$

was chosen and the coefficients $a_n$ were evaluated from the measured field map of the SM3 magnet.

The trajectory is then traced back through the SM12 magnet to the target region using the 'SM3 momentum'. The field of the SM12 magnet is also given by functions of $x$ and $y$ coordinates. For trajectories origina.ing from the target, their momenta are re-evaluated with the added constraint that the trajectories originate from the target center using an iterative method (called 'SM12 momentum'). The details of the trace back and momentum reconstruction appear in Appendix II.

**Momentum Resolution**

As described above, the 'SM3 momentum' is calculated using the trajectory of the particle obtained by fitting the hit positions in the chambers. Since our chambers are placed close together within one station, the coordinates of the trajectory at each station can be expressed at a single plane by neglecting the spacing between the chambers. Also the momentum can be expressed by a linear combination of the mean position at the stations 1, 2 and 3. Using this expression, the momentum resolution is calculated and is shown in Fig. 13 (a). The following three contributions are considered:

i) The spatial resolution of the chambers.
The spatial resolution at each station is approximated by

$$\sigma_{STNi} = \frac{\sigma_i}{\sqrt{\bar{N}_i}}, \tag{7}$$

where $\sigma_i$=the spatial resolution of one chamber in the $i$-th station ($2/\sqrt{12}$ mm for station 1, and 200 micron for stations 2 and 3).
$\bar{N}_i$=average number of chambers registering in the $i$-th station (5.3, 5.47 and 5.02 for stations 1, 2 and 3, respectively).

ii) The multiple scattering due to the materials in stations 1, 2 and the Cherenkov mirrors.

iii) The deviation of the $z$ position of the SM3 bend plane from the standard bend plane.

The resolution of the 'SM3 momentum' mainly arises from the chamber resolution, especially that of station 1. The error in the 'SM3 momentum' causes an error in the $y$ position of the trajectory when the trajectory is traced back to the target position. The momentum resolution estimated from the width of the $y$ distribution at the target is also shown in Fig. 13 (a). This resolution agrees well with the calculated value.

The 'SM12 momentum' is determined by tracing back the trajectory up to the target and by constraining the trajectory to originate from the center of the target. Using the same approximation for the coordinates of the trajectory in each station, the 'SM12 momentum' can be expressed by a linear combination of the $y$ positions at stations 2 and 3. The expression also includes the integral of the magnetic field along the trajectory which depends on the $y$ position at stations 2

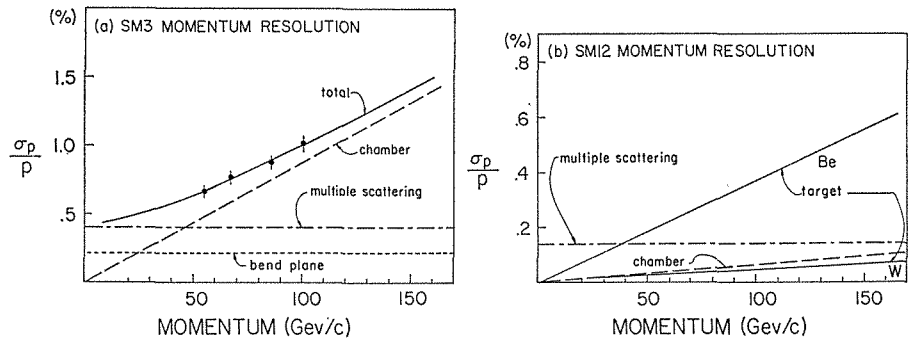


Fig. 13. Momentum resolution as a function of momentum.
(a) 'SM3 momentum'
(b) 'SM12 momentum'
The *contributions denoted are*;
chamber: error due to the spatial resolution of the chambers,
multiple scattering: error due to the multiple scattering in material between station 1 and 3,
bend plane: error due to the deviation of the $z$ position of the bend plane from the standard value for the SM3 magnet,
target Be and W: error due to the variation of the production point along $z$ direction in the Be and W target, respectively.
The data points (●) in (a) show the resolution estimated from the width of the $y$ distribution at the target in the trace back.

and 3, however this dependence can be neglected in the calculation of the momentum resolution. The results of the calculation are shown in Fig. 13 (b). The contribution of the chamber resolution is negligibly small in this case. Since the trajectories are assumed to originate from the center of the target, the finite length of the target also contributes to the resolution. Especially for the Be target, which is 8 times longer than the W target, the contribution due to the target length becomes the largest contribution to the resolution. The use of the SM12 magnet and the target constraint improves the momentum resolution by a factor of 2 to 5 depending on which target and momentum are considered.

## C. Event Selection

Several cuts were applied successively to select good single hadron production events. All the cuts applied are listed in Table 11.

### Single Track Requirement

To study inclusive production, events which include two or more tracks must be counted. However, the detection efficiency of the calorimeter due to energy threshold depends differently on momentum for single and multi particle events. Therefore, only events having a single track in the aperture are selected. It was found that the fraction of events with more than one track in the aperture was 1.38, 1.21, and 1.21% for Be, Cu, and W target, respectively. These values are quite small because our acceptance covers only the high $P_t$ and high momentum region.

Table 11. Cuts for single hadron selection.

1. Single track found in the aperture.
2. Track confidence level cut.

| Number of chambers | C.L. cut |
|---|---|
| 12 | $1.0\times10^{-3}$ |
| 13 | $1.8\times10^{-4}$ |
| 14 | $6.2\times10^{-5}$ |
| 15 | $2.0\times10^{-5}$ |
| 16–18 | $1.0\times10^{-5}$. |

3. Trigger matrix requirement.
4. Hadron cuts;
   i) $|E_{cal}-p|<3\sigma_E$,
   ii) $E_{EM}/E_{cal}<0.94-0.00933\times\ln(p/40)$,
   $E_{Hd}/E_{cal}<0.05-0.01498\times\ln(p/40)$,
   iii) less than 2 hits among Y4, PTX, and PTY.
5. Target cut;
   $|Y(z=\text{target center})-Y_{target}|<2.16$ cm,
   $|X(z=\text{target center})|<1.9$ cm.
6. Fiducial cuts.

**Track Confidence Level Cut**

Events having tracks with a poor confidence level for the track fit were cut out; most such tracks were formed from accidental hits in the chambers. Tracks with a small number of hits in the chambers also likely include tracks of the above category. Therefore, different values of the confidence level cut were used, depending on the number of the chambers having hits on the track. The values of the cuts used are listed in Table 11.

**Trigger Matrix Requirement**

Our trigger system required that the events satisfy at least one of the trigger matrix combinations. However, there are some events in which the recorded trajectory does not satisfy the matrix combinations, but a matrix combination was satisfied due to additional accidental hodoscope hits. The dominant topology of such events are as follows;

i) There are many muons produced in the beam dump. The trajectories of these muons do not satisfy the matrix combinations, since these muons pass through the beam dump. These events are accepted when these muons deposit large energy in the calorimeter and additional accidental hodoscope hits satisfy a matrix combination.

ii) Sometimes, there is an inefficient hodoscope counter along the trajectory of a particle which should satisfy a matrix combination. However, these events often have a high probability of satisfying a matrix combination by an additional accidental hit.

We select events with trajectories which satisfy the matrix and in which all hodoscope counters along the trajectories have fired. 89% of the events from the Be

target and 93% of the events from the Cu and W target pass this requirement.

**Hadron Cuts**

The information from the calorimeter and the detectors at station 4 was used to select hadrons. The following criteria were applied;

i) The energy measured by the calorimeter ($E_{\rm cal}$) must coincide with the momentum measured by the spectrometer ($p$) within three standard deviations of the calorimeter resolution. That is to say,

$$|E_{\rm cal}-p|<3\sigma_E=3.76\times\sqrt{p} \tag{8}$$

The distribution of $(E_{\rm cal}-p)/\sqrt{p}$ is shown in Fig. 14.

ii) Electrons deposit most of their energy in the electromagnetic (EM) part of the calorimeter. Therefore, the following conditions were chosen to define and hence reject electrons.

$$\begin{aligned}&\frac{E_{EM}}{E_{\rm cal}}>0.94-0.00993\times\ln\frac{p}{40},\\ &\frac{E_{EI}}{E_{\rm cal}}>0.05-0.01498\times\ln\frac{p}{40},\end{aligned} \tag{9}$$

where $E_{EM}$ and $E_{EI}$ denote the energies deposited in the EM part and the first module of the EM part of the calorimeter, respectively.

iii) Trajectories were extrapolated to the station 4 hodoscopes and proportional

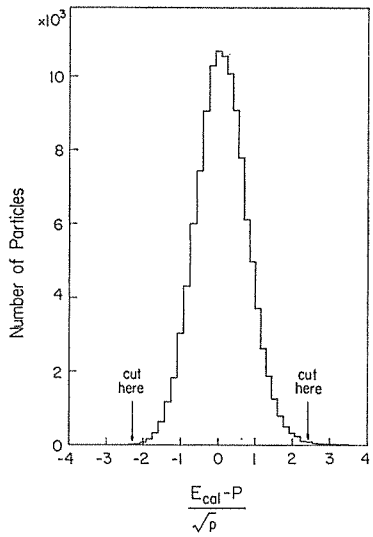


Fig. 14. Distribution of $(E_{\rm cal}-p)/\sqrt{p}$ used for the hadron cut. $E_{\rm cal}$ is the energy measured by the calorimeter, and $p$ is the momentum of the particle measured by the spectrometer.

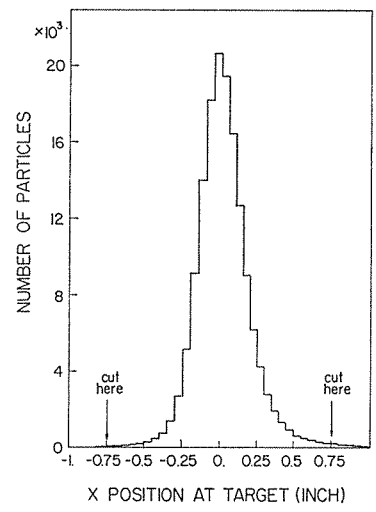


Fig. 15. Distribution of the $x$ position of single hadrons at the target for Cu target data.

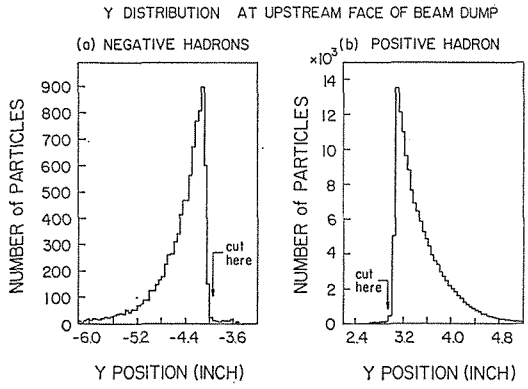


Fig. 16. *Y* distribution of single hadrons at the upstream face of the copper beam dump for the Cu target data.
(a) negative hadrons,
(b) positive hadrons.

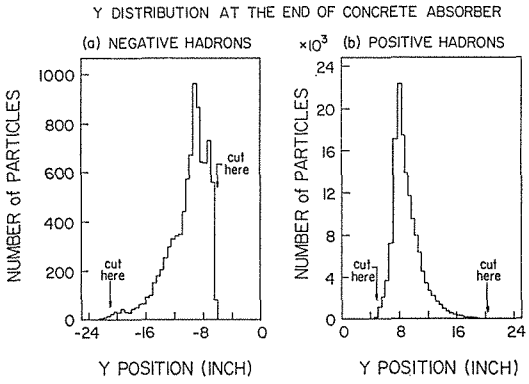


Fig. 17. *Y* distribution of single hadrons at the downstream end of the concrete absorber for the Cu target data.
(a) negative hadrons,
(b) positive hadrons.

tube planes. Then, muon acceptance windows at these planes were calculated taking into account the multiple scattering in the calorimeter and absorber. Tracks which matched with hits within the windows on two or more out of these three planes were cut out. This eliminates muons which deposit most of their energy in the calorimeter by interactions such as deep inelastic scattering or bremsstrahlung.

**Target and Fiducial Cuts**

The trajectories of the particles were checked at the production target using the 'SM3 momentum' to trace through the SM12 magnet. Cuts in the Y and X coordinates were applied at the target position. These cuts reject hadrons produced at the beam dump or magnet walls by secondary particles. These cuts reduce the events by about 15% (Be) to 12% (Cu and W) of the total hadron events. Finally, fiducial cuts were applied at various positions along the trajectory to make sure the tracks passed through well defined apertures. Cuts were made at the upstream face of the beam dump, the last brick absorber in the SM12 magnet, the end of the concrete absorber, the hodoscope planes at each of the stations 1, 2, and 3, and the upstream face of the H2 models of the calorimeter. The dimensions of these aperture cuts are listed in Table 12. The fiducial cut at the calorimeter was made to insure that the energy leakage of the shower from the edge of the sensitive volume

Table 12. Fiducial cuts

| Position | $X$ (cm) | | $Y$ (cm) | |
|---|---|---|---|---|
| | low | high | low | high |
| Upstream face of beam dump | — | — | −9.91* | 7.49* |
| Last lead brick | — | — | −53.7 | 51.4 |
| End of the concrete absorber | — | — | −16.8* | 12.4* |
| Y1 hodoscope | −58.8 | 61.8 | −75.3 | 75.8 |
| Y2 hodoscope | −79.4 | 81.9 | −84.9 | 86.6 |
| Y3 hodoscope | −131.7 | 131.2 | −115.5 | 116.9 |
| Upstream face of H2 calorimeter | −137.2 | 137.2 | −121.9 | 121.9 |
| | −5.08* | 5.08* | — | — |

Note) The cuts with * mean that the events are cut out if the positions of the trajectories are between the values of low and high

Table 13. Summary of the results of the various cuts.

| Cuts | Be | | Cu | | W | |
|---|---|---|---|---|---|---|
| | passed | failed | passed | failed | passed | failed |
| Triggers | 158,191 | | 226,399 | | 219,491 | |
| Track found by tracker | 132,192 | 25,999 | 204,889 | 21,510 | 197,899 | 21,592 |
| More than one tracks | 130,360 | 1,832 | 202,406 | 2,483 | 195,498 | 2,401 |
| Track C.L. cut | 127,560 | 2,800 | 199,614 | 2,792 | 192,673 | 2,825 |
| Trigger matrix requirement | 110,379 | 17,181 | 184,075 | 15,539 | 178,087 | 14,586 |
| Hadron cuts | 108,258 | 2,121 | 181,746 | 2,329 | 175,867 | 2,220 |
| Target Y cut | 85,337 | 22,921 | 152,215 | 29,531 | 148,585 | 27,282 |
| Target X cut | 83,936 | 1,401 | 150,435 | 1,780 | 146,881 | 1,704 |
| SM12 aperture cut | 82,955 | 981 | 149,415 | 1,020 | 145,922 | 959 |
| X fiducial cuts | 80,849 | 2,106 | 145,539 | 3,876 | 142,266 | 3,656 |
| Y fiducial cuts | 80,525 | 324 | 144,985 | 554 | 141,702 | 564 |
| Fraction of events passed all cuts | 0.509 | | 0.640 | | 0.645 | |

or the gap between the left and right sides was negligibly small. The $x, y$ distribution of valid trajectories at several $z$ positions is shown in Figs. 15, 16, and 17 for Cu target data. These distributions for other targets are almost the same.

The results of the successive cuts are summarized in Table 13 for each target. The fraction of the events which passed all the cuts was 51% for Be, and 64% for Cu and W targets.

## D. Background

The cuts described in the previous section select mostly events containing single hadrons produced at the target. However the selected events also contain some background events. Those background events are divided into two types. The first type is electron or muon events which are misidentified as hadrons. The second type is hadrons which are not produced at the target but somewhere else and whose

trajectories are still consistent with the target due to the finite error in the trace back.

The contamination of these background events is estimated in the following manner.

**Electron Contamination**

Single electron events which are positively identified as electrons as described in the previous section amount to 0.289, 0.146 and 0.126% of the single hadron events for the Be, Cu, and W targets, respectively. Since the efficiency of the electron identification is estimated to be about 95%, the contamination of electrons in the single hadron events should be about 0.014, 0.007 and 0.006% for the Be, Cu and W targets, respectively. These are negligibly small.

**Muon Contamination**

Muon contamination is estimated in the following way. First, the data were analyzed with the same procedure except requiring hits on 2 or more planes in station 4, instead of 1 or no planes as in the hadron selection case. This procedure selects events with muons which loose most of their energy in the calorimeter by interaction but still continue along the incident trajectory (called Case A). The ratio of these muon events to single hadron events is $0.016 \pm 0.008$, $0.056 \pm 0.013$ and $0.031 \pm 0.010$% for the Be, Cu, and W targets, respectively. Misidentification of muons as hadrons can happen when the muon emerges with a large angle with respect to the incident trajectory after an interaction in the calorimeter and misses the muon identification window in station 4 (called Case B). The ratio of Case B events to Case A events is obtained using events with muons produced in the beam dump. These muon events are selected by requiring that the trajectories originate in the beam dump and traverse the concrete absorbers in the SM12 magnet. The ratio of Case B to Case A events is found to be about 0.4 almost independent of the momentum of the muons. Therefore the contamination of muon events is calculated to be 0.006, 0.022, 0.012% for the Be, Cu, and W targets, respectively. These are also negligibly small.

**Hadron Background (Target Out Data)**

Background hadrons which are produced at other places than the target by the incident beam can be measured by the target out run. The target out data were taken with $0.9 \times 10^{12}$ equivalent protons on the target. This number of protons amounts to 4.0, 3.6 and 5.5% of the total number of protons on the Be, Cu and W targets, respectively. The target out data were analyzed with the same procedure as the metal target data. It has been found that the overall rate of events which pass all the cuts is 0.62, 0.40, and 0.26% of the Be, Cu and W rates, respectively. These hadrons are presumably produced at the target holder or at the window of the beam pipe in the upstream of the target.

The corrections for the above backgrounds were not made in the present analysis because they are negligibly small.

**Hadron background (Tertiary Hadrons)**

The hadrons produced from the target at small angles hit the beam dump and produce tertiary hadrons. When those tertiary hadrons are produced near the surface of the beam dump with high enough momentum, the trajectories of these hadrons can be similar to those of hadrons produced directly from the target. Since the trace back has some error mainly due to the error in the 'SM3 momentum', the trajectories of these tertiary hadrons can be consistent with a target origin. In order to estimate the fraction of events containing tertiary hadrons, the $y$ distributions at the target are examined for events which pass all other cuts. These distributions are shown in Fig. 18. The distributions show clear peaks at the target position and the tails of the background events. The shape of the distribution of the background depends on $P_t$ and $\theta^*$. The number of the target events is estimated by

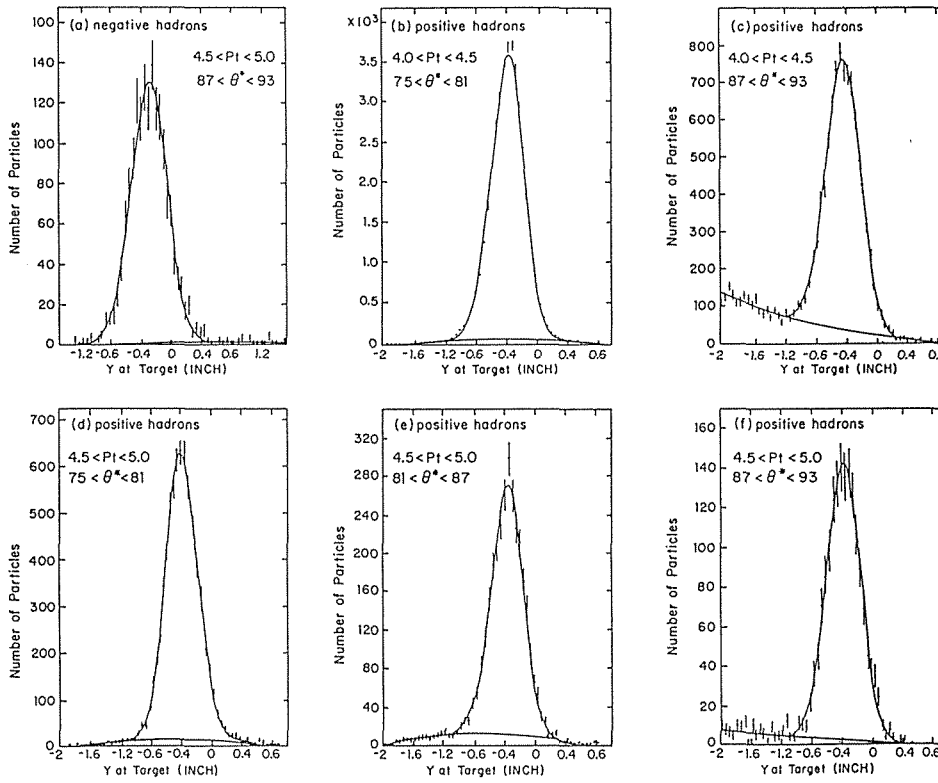


Fig. 18. $Y$ distribution of single hadrons at the target.
The curves obtained from the fit described in the text are superimposed. The two curves in each figure show the background contribution and sum of the signal and background, respectively.
(a) negative hadrons, $4.5<P_t<5.0$ Gev/c, $87<\theta^*<93°$,
(b) positive hadrons, $4.0<P_t<4.5$ Gev/c, $75<\theta^*<81°$,
(c) positive hadrons, $4.0<P_t<4.5$ Gev/c, $87<\theta^*<93°$,
(d) positive hadrons, $4.5<P_t<5.0$ Gev/c, $75<\theta^*<81°$,
(e) positive hadrons, $4.5<P_t<5.0$ Gev/c, $81<\theta^*<87°$,
(f) positive hadrons, $4.5<P_t<5.0$ Gev/c, $87<\theta^*<93°$.

fitting the distribution with a Gaussian distribution for the target events and a quadratic polynomial for the background. The curves obtained by fitting are also shown in Fig. 18. The curves fit the data quite well. The fraction of background events varies from 0.1 to 15% depending on the kinematic region. A correction is made for these background events. There is no reason for the shape of the background to be quadratic polynomial. The quadratic form is chosen because this form is simple and fits the data well. However, it should be noted that the shape of the distribution is very similar for different targets in the same kinematic region. Therefore the ratio of target events from the various targets is insensitive to the assumed shape of the background distribution.

### E. Normalization

The number of events can be expressed in terms of the transverse momentum $P_t$ and the polar angle $\theta^*$ in the C.M. system, as follows;

$$N(P_t, \theta^*) = N_B \cdot N_T \int_{P_{t_1}}^{P_{t_2}} dP_t \int_{\theta_1^*}^{\theta_2^*} d\theta^* \frac{p^{*2}}{E^*} \frac{E d\sigma}{d^3p} \mathrm{Acc}(P_t, \theta^*) \cdot \varepsilon \cdot \varepsilon_{\mathrm{TRIG}} \cdot \varepsilon_{\mathrm{SOFT}} ,$$

$$\simeq N_B \cdot N_T \frac{\bar{p}^{*2}}{\bar{E}^*} \frac{E d\sigma}{d^3p} \overline{\mathrm{Acc}} \cdot \bar{\varepsilon} \cdot \bar{\varepsilon}_{\mathrm{TRIG}} \cdot \bar{\varepsilon}_{\mathrm{SOFT}} \cdot \Delta P_t \cdot \Delta\theta^* , \tag{10}$$

where $N_B$=total number of protons incident on the target,

$N_T$=number of target nuclei per unit area, given by

$$N_T = \frac{N_a \cdot \rho \cdot L}{A} , \tag{11}$$

where $N_a$ is Avogadoro's number, $\rho$ and $L$ are the density and length of the target,

$p^*$, $E^*$=the momentum and energy of the produced particles in the C.M.S,

$Acc(P_t, \theta^*)$=geometrical acceptance,

$\varepsilon$=correction due to the absorption of particles in the target and the decay of hadrons in flight,

$\varepsilon_{\mathrm{TRIG}}$=triggering efficiency,

$\varepsilon_{\mathrm{SOFT}}$=off-line software reconstruction and cut efficiency,

$\Delta P_t$, $\Delta\theta^{**}$=bin width in $P_t$ and $\theta^*$,

and the quantities with a bar on top mean the average within the bin. $\varepsilon$, $\varepsilon_{\mathrm{TRIG}}$, and $\varepsilon_{\mathrm{SOFT}}$ also depend on $P_t$ and $\theta^*$. In fact $\varepsilon_{\mathrm{TRIG}}$ had a strong dependence on $P_t$ an $\theta^*$ due to the threshold of the calorimeter. If one takes a ratio of the cross-sections for different targets, many factors such as acceptance, $\varepsilon_{\mathrm{TRIG}}$, and $\varepsilon_{\mathrm{SOFT}}$ cancel out, since these data were taken with the same apparatus and analyzed by an identical procedure. Therefore, for the $A$-dependence analysis, one only has to concentrate on the terms which vary depending on the target, such as the integrated luminosity ($N_B \cdot N_T$) etc. The following correction factors were applied to evaluate the $A$-dependence.

**Integrated Luminosity**

The intensity of the incident beam hitting the target was monitored by the 90 degree monitor throughout the experiment. Since the response of the 90 degree monitor depends on the target, the ratio of the counts in the 90 degree monitor to SEM counts was measured for all targets. The SEM counts all the incident protons, on the other hand the 90 degree monitor counts only the part of the protons because the beam profile is wider than the target thickness as shown in Fig. 3 (b). Therefore, the measured ratio was corrected for the fraction of the beam hitting the target. The absolute intensity of the incident beam was measured by using a copper and aluminum foil irradiation. It was found that one count in the 90 degree monitor corresponded to $1.50\times10^{7}$ protons on the Be target. The results of the measurements and the integrated luminosity are listed in Table 14.

Table 14. Integrated luminosities

| | Targets | | |
|---|---|---|---|
| | Be | Cu | W |
| $\frac{\text{90 degree mon.}}{\text{SEM}}$ * 100% | 30.8 | 70.5 | 99.6 |
| Total 90 degree monitor counts | $1.456\times10^{6}$ | $3.658\times10^{6}$ | $4.076\times10^{6}$ |
| Be equivalent 90 degree monitor counts | $1.456\times10^{6}$ | $1.60\times10^{6}$ | $1.26\times10^{6}$ |
| Total number of protons | $2.20\times10^{13}$ | $2.40\times10^{13}$ | $1.89\times10^{13}$ |
| Number of nuclei in the target ($cm^{-2}$) | $1.258\times10^{24}$ | $2.198\times10^{13}$ | $8.258\times10^{22}$ |
| Integrated luminosity ($cm^{-2}$) | $2.87\times10^{37}$ | $5.25\times10^{36}$ | $1.56\times10^{36}$ |
| Ratio of the integrated luminosity to Be | 1.0 | 0.19 | 0.056 |

*) These ratios are corrected with the target efficiencies

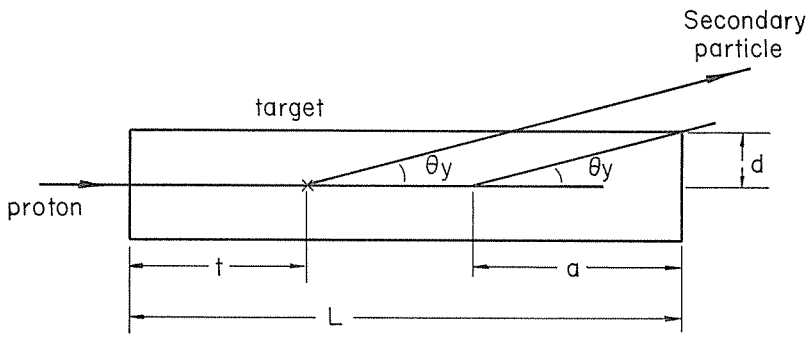


Fig. 19. Illustration of the absorption calculation in the target.

**Absorption of Beam and Produced Particles in Target**

As shown in Fig. 19 for our target geometry, the incident protons traverse a distance $t$ in the target before they interact. The produced particles at angle $\theta_y$ can also be absorbed before leaving the target. Therefore, the reduction factor $F_{abs}$ can be expressed for our target geometry;

$$F_{\mathrm{abs}}(\theta_y, t) = \begin{cases} e^{-t/\lambda_b} \cdot e^{-a/\lambda_i} & \text{if } t > L-a\,, \\ e^{-t/\lambda_b} \cdot e^{-(L-t)/\lambda_i} & \text{if } t < L-a\,, \end{cases} \tag{12}$$

where $\lambda_b$=absorption length for the incident beam,
$\lambda_i$=absorption length for the produced particle of type $i$,
$a=d/\tan(\theta_y)$, $d$ is half thickness of the target,
$L$=length of the target.

Assuming that the incident beam traverses the center line of the target, the average reduction factor can be obtained by integrating $F_{\mathrm{abs}}(\theta_y, t)$ over $t$;

$$\begin{aligned} \bar{F}_{\mathrm{abs}}(\theta_y) &= \frac{1}{L}\int_0^L F_{\mathrm{abs}}(\theta_y, t)\mathrm{d}t \\ &= e^{-a/\lambda_i}\frac{\lambda_b}{L}\left(1-e^{-\frac{L-a}{\lambda_b}}\right)+e^{-\frac{L-a}{\lambda_b}}e^{-\frac{a}{\lambda_i}}\frac{\lambda_b\lambda_i}{L(\lambda_i-\lambda_b)}\left\{1-e^{-a\left(\frac{1}{\lambda_b}-\frac{1}{\lambda_i}\right)}\right\} \end{aligned} \tag{13}$$

The correction due to this factor was made as a function of $P_t$ and $\theta^*$. Since the TY·Hhi trigger events include the production of pions, kaons and protons, the correction factors are calculated using an appropriate weiieightp for ions, kaons and protons according to the particle ratios. The factors are listed in Table 15.

**Track Finding Effciency**

At thc beginning of the data taking, the efficiency of some of the chambers varied in a relatively short period due to the lack of stability of the gas circulation. The track finding efficiency depends crucially on the chamber efficiencies, and also depends on the counting rates due to multiple hits especially in the drift chambers. Since our drift chamber readout system does not have multiple hit capability, drift time information can be lost due to another hit on the same wire. The Be target produces about 40% higher singles rates than the W target as shown in Table 9. The chamber efficiency was estimated from the data in the following manner. The efficiency of the $i$-th chamber in station $m$ can be expressed by assuming no correlation between the chambers:

$$\varepsilon_i = \frac{N_i}{N_0+N_i}\,, \tag{14}$$

where $N_0$=number of tracks which fire all chambers in station $m$,
$N_i$=number of tracks which fail to fire only the $i$-th chamber in station $m$.
However, there is an additional inefficiency due to the correlation between two chambers in the same station. This inefficiency $\delta_{ij}$ can be expressed by;

$$\begin{aligned} \delta_{ij} &= \frac{r_i \cdot r_j - r_{ij}}{1+r_i+r_j+r_{ij}}\,, \\ r_i &= \frac{N_i}{N_0}\,, \quad r_{ij} = \frac{N_{ij}}{N_0}\,, \end{aligned} \tag{15}$$

where $N_{ij}$=number of tracks which fail to fire chambers $i$ and $j$ in station $m$.

Table 15. Correction factors due to absorption in the targets.

| Target | $\theta^*$(deg) / $\theta_y$(rad) | 60.0 .0396 | 65.0 .0437 | 70.0 .0480 | 75.0 .0526 | 80.0 .0575 | 85.0 .0628 | 90.0 .0686 | 95.0 .0749 | 100.0 .0818 | 105.0 .0894 | 110.0 .0981 | 115.0 .1078 | 120.0 .1191 |
|---|---|---|---|---|---|---|---|---|---|---|---|---|---|---|
| Be | average | .8729 | .8745 | .8759 | .8772 | .8783 | .8793 | .8803 | .8812 | .8820 | .8827 | .8834 | .8841 | .8848 |
| | $\pi^-$ | .8732 | .8748 | .8762 | .8774 | .8785 | .8795 | .8805 | .8813 | .8821 | .8829 | .8836 | .8842 | .8849 |
| | $K^-$ | .8749 | .8763 | .8776 | .8787 | .8797 | .8806 | .8815 | .8822 | .8830 | .8836 | .8843 | .8849 | .8854 |
| | $\bar{P}$ | .8651 | .8674 | .8694 | .8712 | .8728 | .8743 | .8756 | .8769 | .8780 | .8791 | .8801 | .8811 | .8820 |
| | average | .8725 | .8741 | .8755 | .8768 | .8780 | .8790 | .8800 | .8809 | .8817 | .8825 | .8832 | .8839 | .8846 |
| | $\pi^+$ | .8733 | .8748 | .8762 | .8774 | .8786 | .8796 | .8805 | .8814 | .8821 | .8829 | .8836 | .8843 | .8849 |
| | $K^+$ | .8760 | .8774 | .8785 | .8796 | .8805 | .8814 | .8822 | .8829 | .8835 | .8842 | .8848 | .8853 | .8859 |
| | $P$ | .8673 | .8693 | .8712 | .8728 | .8743 | .8757 | .8769 | .8781 | .8791 | .8801 | .8810 | .8819 | .8828 |
| Cu | average | .8784 | .8813 | .8840 | .8866 | .8890 | .8912 | .8933 | .8953 | .8973 | .8991 | .9008 | .9025 | .9041 |
| | $\pi^-$ | .8788 | .8817 | .8844 | .8869 | .8893 | .8915 | .8936 | .8956 | .8975 | .8993 | .9010 | .9027 | .9043 |
| | $K^-$ | .8814 | .8841 | .8867 | .8891 | .8913 | .8934 | .8953 | .8972 | .8990 | .9007 | .9023 | .9038 | .9053 |
| | $\bar{P}$ | .8669 | .8706 | .8740 | .8772 | .8803 | .8831 | .8858 | .8883 | .8907 | .8930 | .8952 | .8974 | .8994 |
| | average | .8776 | .8805 | .8833 | .8859 | .8884 | .8907 | .8928 | .8949 | .8968 | .8986 | .9004 | .9021 | .9038 |
| | $\pi^+$ | .8788 | .8817 | .8844 | .8869 | .8893 | .8915 | .8936 | .8956 | .8975 | .8993 | .9010 | .9027 | .9043 |
| | $K^+$ | .8834 | .8860 | .8884 | .8907 | .8928 | .8948 | .8966 | .8984 | .9001 | .9017 | .9032 | .9047 | .9061 |
| | $P$ | .8694 | .8729 | .8762 | .8793 | .8821 | .8849 | .8874 | .8898 | .8921 | .8943 | .8964 | .8985 | .9004 |
| W | average | .8774 | .8781 | .8795 | .8813 | .8833 | .8855 | .8878 | .8902 | .8926 | .8950 | .8975 | .8999 | .9024 |
| | $\pi^-$ | .8778 | .8785 | .8799 | .8816 | .8836 | .8858 | .8881 | .8905 | .8929 | .8953 | .8977 | .9001 | .9026 |
| | $K^-$ | .8803 | .8809 | .8822 | .8839 | .8858 | .8879 | .8901 | .8924 | .8947 | .8970 | .8993 | .9016 | .9040 |
| | $\bar{P}$ | .8667 | .8675 | .8691 | .8712 | .8736 | .8762 | .8789 | .8818 | .8846 | .8875 | .8904 | .8934 | .8963 |
| | average | .8766 | .8773 | .8787 | .8805 | .8825 | .8848 | .8871 | .8895 | .8920 | .8944 | .8969 | .8994 | .9019 |
| | $\pi^+$ | .8777 | .8784 | .8798 | .8815 | .8835 | .8857 | .8880 | .8904 | .8928 | .8952 | .8976 | .9001 | .9025 |
| | $K^+$ | .8822 | .8829 | .8841 | .8857 | .8876 | .8896 | .8917 | .8939 | .8961 | .8983 | .9006 | .9028 | .9050 |
| | $P$ | .8687 | .8695 | .8711 | .8731 | .8754 | .8780 | .8806 | .8834 | .8862 | .8890 | .8918 | .8946 | .8975 |

Table 16. Average chamber efficiencies

| Chambers | Targets | | |
|---|---|---|---|
| | Be | Cu | W |
| Y1A | .8039 | .8949 | .8313 |
| U1A | .4675 | .6708 | .6831 |
| V1A | .8902 | .8754 | .8775 |
| Y1B | .9291 | .9323 | .9356 |
| U1B | .9443 | .9495 | .9509 |
| V1B | .9279 | .9365 | .9364 |
| Y2 | .9379 | .9434 | .9411 |
| Y2′ | .9619 | .9667 | .9652 |
| U2 | .9021 | .9089 | .9068 |
| U2′ | .9450 | .9505 | .9511 |
| V2 | .9252 | .9313 | .9301 |
| V2′ | .9452 | .9511 | .9506 |
| Y3 | .8193 | .8227 | .8256 |
| Y3′ | .7901 | .7946 | .7977 |
| U3 | .8746 | .8819 | .8835 |
| U3′ | .8788 | .8854 | .8870 |
| V3 | .8349 | .8413 | .8438 |
| V3′ | .8941 | .9024 | .8996 |
| Tracker | .9430 | .9704 | .9634 |

This inefficiency occurs when two particles traverse the same drift cells in a pair of drift chambers and depends on the instantaneous intensity. The track finding efficiency for each run was calculated including these correlated efficiencies. The average efficiencies of the chambers are listed in Table 16.

**Single Particle Acceptance**

As described above, the geometrical acceptance is cancelled out in evaluating the $A$-dependence of single hadron production. However it might be useful to describe it here briefly to help understand the experiment. Fig. 20 shows our geometrical acceptance in $P_z$—$P_y$ momentum space in the laboratory system for single particles produced at the target. The asymmetry of the acceptance for positive and negative particles is mainly due to the finite angle between the incident beam and the axis of the spectrometer system. Horizontally, the acceptance is about $\pm 28$ milliradians in the laboratory system. Fig. 21 shows the polar angle acceptance versus $P_y$ in the center of mass system of the proton and nucleon.

## F. Cheremkov Events

In addition to the corrections described above, other corrections and cuts were necessary for Cherenkov events.

As mentioned above, generally the detector efficiency need not be taken into

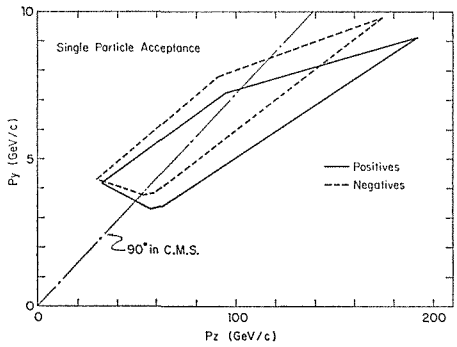


Fig. 20. Single particle acceptance in $P_y-P_z$ momentum space in the laboratory system.

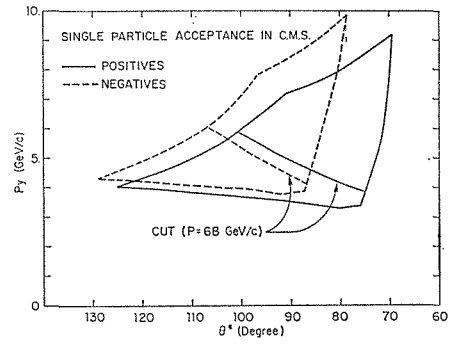


Fig. 21. Single particle acceptance in the C.M. system in $P_y-\theta^*$ momentum space.

account to evaluate the $A$-dependence. Nevertheless the Cherenkov counter efficiency must be taken into account with two reasons;

i) The efficiency of the photon detector varied appreciably during the early stages of the run so that the average number of photons per pion fluctuated run by run.

ii) Since the Cherenkov threshold for protons was quite high (about 118 Gev/c), most of the protons in our momentum acceptance were not fast enough to be identified. Therefore the yield of protons had to be evaluated by subtracting the pion and kaon yield from the total number of events. In order to do the subtraction correctly, the number of pions and kaons must be corrected for the efficiency of identification.

**Geometrical Effciency**

Some fraction of the Cherenkov photons miss the mirror when the particles pass close to the edge of a mirror. Also there is some inefficiency due to the gap between the mirror arrays (about 2 cm). The efficiency ($\varepsilon_{\mathrm{GEOM}}$) can be calculated for a given trajectory and particle type;

$$\varepsilon_{\mathrm{GEOM}} = \int_0^L e^{-l/\lambda} \cdot F_\phi(r_M, x_M, y_M)\,\mathrm{d}l \Big/ \int_0^L e^{-l/\lambda}\mathrm{d}l\,, \tag{16}$$

where $L$=path length of the particle from the upstream face of the helium tank to the mirror,

$\lambda$=absorption length of the photon in the radiator gas,

$r_M = l \cdot \tan(\theta_c)$=radius of the photon at the mirror, $\theta_c$ is the Cherenkov radiation angle,

$x_M, y_M$=position of the particle trajectory at the mirror.

$F_\phi(r_M, x_M y_M)$ is the ratio of the arc at the mirror to the whole ring having a center at $x_M, y_M$ and radius $r_M$ at the mirror, and is calculable knowing the mirror geometry. The absorption length of the photon in the radiator gas was measured using the UV source [57] about once a day during the run. The absorption was found to be stable within 2% and gave $\lambda$=82.7 m.

**Particle Identification Efficiency**

As described earlier the distribution of the number of photons detected in the photon detector shows a Poisson distribution. Therefore, the inefficiency due to zero photons for events having $\bar{n}$ photons on the average is given by $e^{-\bar{n}}$. For Cherenkov radiation, the following relations are known;

$$\bar{n} \propto \sin^2 \theta_c ,$$
$$\sin^2 \theta_c = 1 - \left(\frac{1}{n\beta}\right)^2 = \frac{\Delta - a}{1+\Delta}, \tag{17}$$

where $n$=refractive index of radiator,
$\Delta = n^2 - 1$,
$\beta$=velocity of the particle,
$a = m^2/p^2$ with $m$ and $p$ being the mass and momentum of the particle respectively.

Using the above relations, the average number of photons for a given particle can be expressed by,

$$\bar{n} = n_0 \cdot \frac{\Delta - a}{\Delta} \cdot \varepsilon_{\mathrm{GEOM}} , \tag{18}$$

where $n_0$ is the average number of photons for a particle with $\beta = 1$ whose photons were contained on a single mirror ($\varepsilon_{\mathrm{GEOM}} = 1$). $n_0$ was obtained for each run from pion events contained on a single mirror. The efficiency was calculated event by event for identified events and each event was weighted by the inverse of the efficiency. A correction due to the dead time of the photon chamber caused by sparking was also made. The dead time was estimated to be about 10, 7, and 6% for the Be, Cu, and W targets, respectively. In the following cases, the particle can not be identified.

i) For high momentum pions or kaons, the radii of photons coincide within the error.

ii) The photon hits spread into two rings expected from two types of particles.

In both cases the event was assigned to two possible hadrons weighted according to the confidence level.

**Momentum and Mirror Cuts**

To avoid events with unreasonably large weights, two cuts were imposed on the Cherenkov events.

i) Only events with tracks which hit the mirror (including the gap) were selected. Furthermore, events which had tracks that hit the four corner regions were cut out so that all the selected events have a geometrical efficiency greater than 50%.

ii) The Cherenkov counter efficiency approaches zero at threshold momentum (for kaons about 58 Gev/c). In order to keep the efficiency reasonably high, only particles with momentum higher than 68 Gev/c were selected. A

considerable fraction of $\theta^*$ acceptance in the low $P_t$ region is eliminated by this momentum cut, as shown in Fig. 21.

These cuts reduce the average weight to about 1.15 for pions, and 1.6 for kaons.

**Decay in Flight Correction**

The correction due to the decay in flight of hadrons is necessary to evaluate particle ratios, though the $A$-dependence does not require the correction. The correction must be made for hadrons which decay between the target and the calorimeter, because these hadrons are rejected either in the trigger or in the analysis for the following reasons.

The pions and kaons which decay into muons before the calorimeter do not satisfy the hadron trigger, because the muons deposit only a small energy in the calorimeter.

The kaons which decay into pions can satisfy the hadron trigger, however, these events are rejected in the analysis. If the kaons decay into pions before the SM3 magnet, the trajectory of these pions can not be traced back to the target due to the constraint between the trajectory and momentum, so that these events are rejected by the target cut. The kaons that decay into pions after the SM3 magnet have a finite probability to pass all the cuts and be accepted as hadron events. However, this probability is calculated to be negligibly small.

The fraction of decays in flight amounts to 1.2% for pions and 8.6% for kaons at a momentum of 70 Gev/c.

## V. RESULTS AND DISCUSSION

### A. Results

As discussed in the previous chapters, there are data with the TY·Hhi trigger (non-Cherenkov data) and data with the Cherenkov trigger (Cherenkov data). The data with the TY·Hhi trigger have no information from the Cherenkov counter, however these two kinds of data are somewhat complementary. The TY·Hhi trigger events are much more abundant than the Cherenkov trigger events. Therefore the TY·Hhi trigger data gave higher statistics and a rather wide angular coverage in the polar angle in the C.M. system. On the other hand, the Cherenkov trigger data give information on each particle type but give statistically poor data in the high $P_t$ region. The Cherenkov trigger data are limited within the narrow polar angle region due to the momentum cut.

**Non-Cherenkov Data**

In order to evaluate the absolute cross-section for single hadron production per nucleus on a Be, Cu, or W target, further corrections for the acceptance and trigger efficiency are necessary. Therefore, values relative to those for the W target are listed in Table 17 and 18 as a function of $P_t$ and $\theta^*$. The errors include only statistical ones. The relative cross-section for the three targets is fit with the following function;

$$\sigma_{A/W}(P_t, \theta^*, A) = \left(\frac{A}{183.35}\right)^{\alpha(P_t,\theta^*)}, \tag{19}$$

where $A$ is the atomic weight. The values for the parameter $\alpha(P_t, \theta^*)$ are determined by the fits, and are listed in Table 19. Fig. 22 shows the relative cross-section and fits for several regions of $P_t$ and $\theta^*$. The cross-sections agree well with the fit straight lines. The dependence of $\alpha$ on $\theta^*$ for several $P_t$ regions is shown in Fig. 23. The Chicago-princeton (CP) data [19] taken at 96 degrees in the C.M.S. are also plotted. The measured values of the $\alpha$'s show no significant dependence on $\theta^*$ in our angular acceptance (70 to 110 degree). Therefore, the cross-sections ($\sigma(P_t, \theta^*, A)$) are integrated over $\theta^*$ within a given $P_t$ bin and $\alpha$ is obtained as a function of $P_t$. The results are listed in Table 20. They are plotted together with

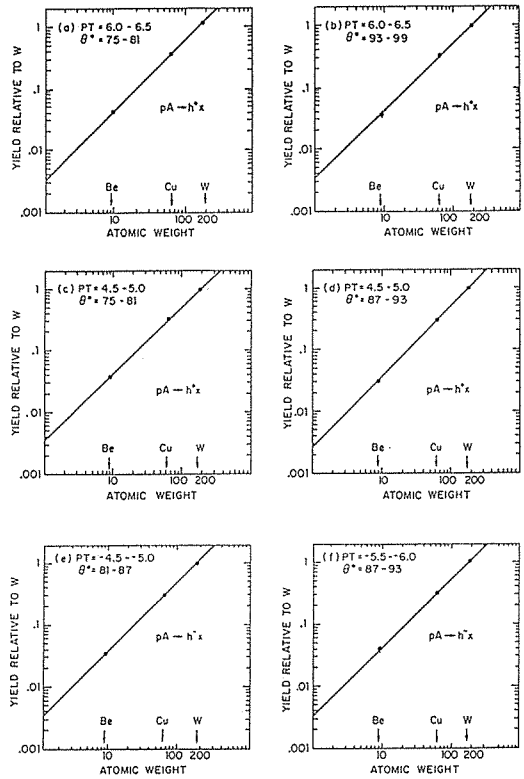


Fig. 22. The cross-section for single hadron production for the Be and Cu targets relative to those for the W target.
The straight lines are the results of the fit;

$$\sigma_{A/W}(P_t, \theta^*, A) = \left(\frac{A}{183.85}\right)^{\alpha(P_t,\theta^*)}$$

(a) positive hadrons, $6.0 < P_t < 6.5$ Gev/c, $75 < \theta^* < 81°$,
(b) positive hadrons, $6.0 < P_t < 6.5$ Gev/c, $93 < \theta^* < 99°$,
(c) positive hadrons, $4.5 < P_t < 5.0$ Gev/c, $75 < \theta^* < 81°$,
(d) negative hadrons, $4.5 < P_t < 5.0$ Gev/c, $87 < \theta^* < 93°$,
(e) negative hadrons, $4.5 < P_t < 5.0$ Gev/c, $81 < \theta^* < 87°$,
(f) negative hadrons, $5.5 < P_t < 6.0$ Gev/c, $87 < \theta^* < 93°$,

the CP data in Fig. 24. The CP data show a slight decrease of $\alpha$ in the high $P_t$ region (above 5 Gev/c), while our data show a rather flat dependence on $P_t$ up to 8 Gev/c. However, the two data sets are consistent within errors.

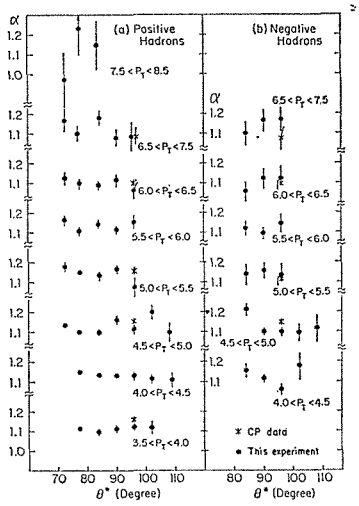


Fig. 23. $\alpha$ versus $\theta^*$ for different regions of $P_t$. (this experiment (●) and the CP measurement (×)).
(a) positive hadrons,
(b) negative hadrons.

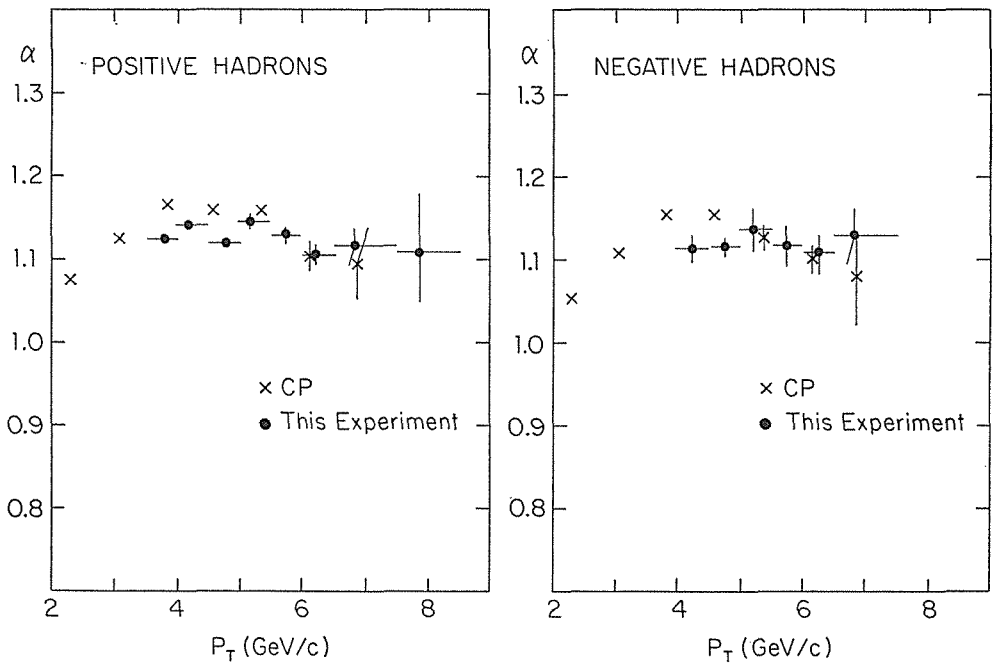


Fig. 24. $\alpha$ versus $P_t$ for this experiment (●) compared with the data of the CP group (×).
(a) positive hadrons,
(b) negative hadrons.

Table 17. The cross-section for single hadron production per nucleus for the Be target relative to the W target.

| Pt (Gev/c) | Positive hadrons | | | | | | | Negative hadrons | | | | |
|---|---|---|---|---|---|---|---|---|---|---|---|---|
| | Polarangle in C.M.S. (degree) | | | | | | | Polar angle in C.M.S. (degree) | | | | |
| | 69~80 | 75~81 | 81~87 | 87~93 | 93~99 | 99~105 | 105~115 | 81~87 | 87~93 | 93~99 | 99~105 | 105~115 |
| 3.5~4.0 | — | .0341 (.0005) | .0366 (.0009) | .0340 (.0009) | .0339 (.0014) | .0357 (.0031) | — | — | — | — | — | — |
| 4.0~4.5 | — | .0319 (.0003) | .0327 (.0009) | .0329 (.0006) | .0320 (.0010) | .0350 (.0021) | .0362 (.0036) | .0335 (.0034) | .0347 (.0013) | .0384 (.0027) | .0285 (.0053) | — |
| 4.5~5.0 | .0319 (.0010) | .0373 (.0008) | .0358 (.0011) | .0313 (.0014) | .0334 (.0023) | .0266 (.0026) | .0346 (.0050) | .0288 (.0022) | .0361 (.0015) | .0361 (.0021) | .0332 (.0035) | .0346 (.0072) |
| 5.0~5.5 | .0284 (.0015) | .0312 (.0010) | .0326 (.0014) | .0315 (.0020) | .0365 (.0045) | — | — | .0323 (.0051) | .0293 (.0033) | .0327 (.0052) | — | — |
| 5.5~6.0 | .0306 (.0020) | .0363 (.0016) | .0325 (.0016) | .0347 (.0023) | .0321 (.0033) | — | — | .0340 (.0034) | .0354 (.0051) | .0364 (.0063) | — | — |
| 6.0~6.5 | .0327 (.0029) | .0355 (.0023) | .0359 (.0024) | .0331 (.0026) | 0.363 (.0046) | — | — | .0399 (.0055) | .0354 (.0051) | .0364 (.0063) | — | — |
| 6.5~7.5 | .0304 (.0044) | .0396 (.0042) | .0286 (.0030) | .0385 (.0046) | .0369 (.0073) | — | — | .0370 (.0064) | .0295 (.0047) | .0327 (.0058) | — | — |
| 7.5~8.5 | .0582 (.0311) | .0251 (.0091) | .0313 (.0014) | — | — | — | — | — | — | — | — | — |

note) The values in the parentheses are statistical errors

Table 18. The cross-section for single hadron production per nucleus for the Cu target relative to the W target.

| Pt (Gev/c) | Positive hadrons | | | | | | | Negative hadrons | | | | |
|---|---|---|---|---|---|---|---|---|---|---|---|---|
| | Polar angle in C.M.S. (degree) | | | | | | | Polar angle in C.M.S. (degree) | | | | |
| | 69~75 | 75~81 | 81~87 | 87~93 | 93~99 | 99~105 | 105~115 | 81~87 | 87~93 | 93~99 | 99~105 | 105~115 |
| 3.5~4.0 | — | .297 (.004) | .301 (.007) | .290 (.007) | .289 (.010) | .289 (.022) | — | — | — | — | — | — |
| 4.0~4.5 | — | .291 (.002) | .292 (.003) | .291 (.005) | .293 (.008) | .311 (.016) | .320 (.027) | .344 (.029) | .298 (.010) | .267 (.017) | .260 (.041) | — |
| 4.5~5.0 | .306 (.008) | .329 (.006) | .293 (.008) | .306 (.011) | .309 (.018) | .287 (.022) | .262 (.033) | .292 (.018) | .272 (.010) | .275 (.015) | .285 (.027) | .377 (.063) |
| 5.0~5.5 | .290 (.016) | .279 (.011) | .297 (.012) | .278 (.016) | .270 (.026) | — | — | .354 (.045) | .265 (.024) | .198 (.033) | — | — |
| 5.5~6.0 | .302 (.016) | .292 (.011) | .287 (.012) | .285 (.016) | .303 (.026) | — | — | .289 (.025) | .300 (.024) | .274 (.030) | — | — |
| 6.0~6.5 | .275 (.021) | .306 (.017) | .331 (.019) | .260 (.018) | .333 (.035) | — | — | .284 (.035) | .282 (.036) | .301 (.046) | — | — |
| 6.5~7.5 | .266 (0.32) | .311 (.029) | .279 (.024) | .288 (.031) | .263 (.047) | — | — | .314 (.047) | .254 (.035) | .230 (.037) | — | — |
| 7.5~8.5 | .740 (.330) | .205 (.063) | .242 (.070) | — | — | — | — | — | — | — | — | — |

note) The values in the parentheses are statistical errors

Table 19. The values of $\alpha$ as a function of $P_t$ and $\theta^*$ for single hadron production.

| $P_t$ (Gev/c) | Positive hadrons | | | | | | | Negative hadrons | | | | |
|---|---|---|---|---|---|---|---|---|---|---|---|---|
| | Polar angle in C.M.S. (degree) | | | | | | | Polar angle in C.M.S. (degree) | | | | |
| | 69~75 | 75~81 | 81~87 | 87~93 | 93~99 | 99~105 | 105~115 | 81~87 | 87~93 | 93~99 | 99~105 | 105~115 |
| 3.5~4.0 | — | 1.126 (.005) | 1.092 (.009) | 1.108 (.009) | 1.121 (.014) | 1.120 (.031) | — | — | — | — | — | — |
| 4.0~4.5 | — | 1.146 (.003) | 1.131 (.004) | 1.131 (.006) | 1.128 (.014) | 1.109 (.020) | 1.108 (.025) | 1.154 (.035) | 1.115 (.013) | 1.058 (.024) | — | 1.118 (.064) |
| 4.5~5.0 | 1.135 (.010) | 1.099 (.007) | 1.095 (.011) | 1.160 (.015) | 1.113 (.023) | 1.202 (.032) | 1.096 (.049) | 1.213 (.027) | 1.097 (.014) | 1.093 (.021) | 1.181 (.062) | — |
| 5.0~5.5 | 1.178 (.018) | 1.146 (.011) | 1.131 (.015) | 1.167 (.023) | 1.074 (.041) | — | — | 1.143 (.049) | 1.158 (.039) | 1.137 (.054) | 1.097 (.037) | — |
| 5.5~6.0 | 1.165 (.022) | 1.104 (.015) | 1.146 (.018) | 1.114 (.023) | 1.153 (.035) | — | — | 1.123 (.035) | 1.093 (.031) | 1.149 (.045) | — | — |
| 6.0~6.5 | 1.124 (.031) | 1.098 (.022) | 1.090 (.022) | 1.114 (.029) | 1.062 (.042) | — | — | 1.056 (.046) | 1.123 (.048) | 1.125 (.057) | — | — |
| 6.5~7.5 | 1.175 (.049) | 1.102 (.038) | 1.185 (.037) | 1.072 (.042) | 1.090 (.070) | — | — | 1.102 (.057) | 1.173 (.054) | 1.173 (.064) | — | — |
| 7.5~8.5 | .975 (.143) | 1.234 (.137) | 1.149 (.120) | — | — | — | — | — | — | — | — | — |

note) The values in the parentheses are statistical errors

Table 20. The values of $\alpha$ as a function of $P_t$ for cross-sections integrated over $\theta^*$.

| $P_t$ (Gev/c) | Positive hadrons | | | Negative hadrons | | |
|---|---|---|---|---|---|---|
| | $\langle P_t \rangle$ (Gev/c) | $\langle \theta^* \rangle$ (degree) | $\alpha$ | $\langle P_t \rangle$ (Gev/c) | $\langle \theta^* \rangle$ (degree) | $\alpha$ |
| 3.5～4.0 | 3.84 | 82.3 | 1.123±.004 | — | — | — — |
| 4.0～4.5 | 4.20 | 81.8 | 1.141±.002 | 4.27 | 90.8 | 1.114±.011 |
| 4.5～5.0 | 4.74 | 80.7 | 1.118±.005 | 4.67 | 91.6 | 1.115±.010 |
| 5.0～5.5 | 5.18 | 80.7 | 1.145±.007 | 5.30 | 90.8 | 1.139±.019 |
| 5.5～6.0 | 5.76 | 82.2 | 1.129±.009 | 5.72 | 90.5 | 1.117±.025 |
| 6.0～6.5 | 6.20 | 82.8 | 1.106±.012 | 6.24 | 91.5 | 1.109±.027 |
| 6.5～7.5 | 6.82 | 82.6 | 1.116±.019 | 6.83 | 91.8 | 1.129±.031 |
| 7.5～8.5 | 7.80 | 88.9 | 1.109±.067 | — | — | — — |

## Cherenkov Data

The relative cross-sections for single hadron production per nucleus on the Be and Cu targets compared to those of the W target are listed in Table 21 for each particle type (as a function of $P_t$). The results for $\bar{p}$ production are not presented, since the $\bar{p}$ yield is small and the yield is consistent with zero within errors. In our case, the subtraction of $\pi^-$ and $K^-$ events due to the Cherenkov counter inefficiency

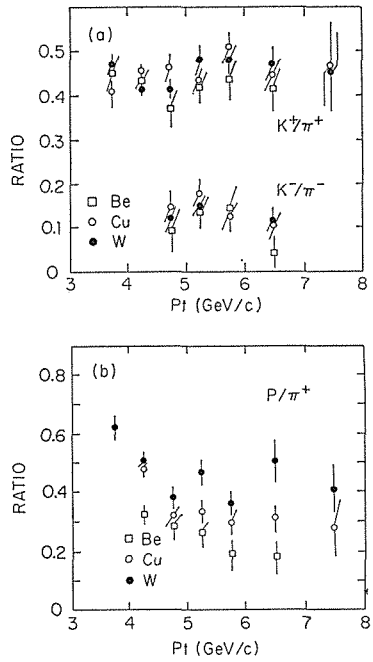


Fig. 25. Particle ratios versus $P_t$.
(a) $K^+/\pi^+$ and $K^-/\pi^-$,
(b) $p/\pi^+$.
The cross, open circle, and closed circle represent the Be, Cu, and W target data, respectively.

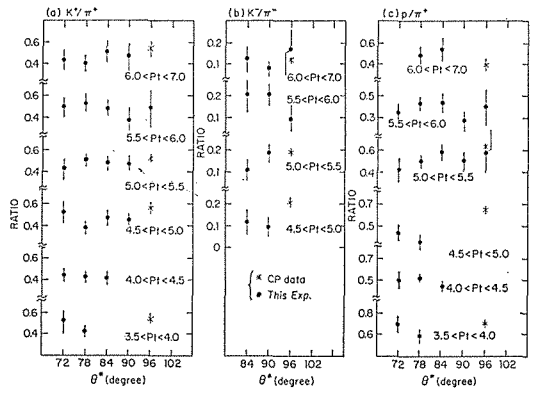


Fig. 26. Particle ratios versus $\theta^*$ for the W target data.
(a) $K^+/\pi^+$,
(b) $K^-/\pi^-$, and
(c) $p/\pi^+$.
(this experiment (●) and the CP measurement (×)).

is much larger than the expected number of $\bar{p}$ events. The ratios of the cross-sections for single kaon and proton production to those for pion production (particle ratios) are listed in Table 22, and shown in Fig. 25. These cross-sections are integrated over the $\theta^*$ acceptance. The errors shown are only statistical. The particle ratios as a function of $\theta^*$ for various $P_t$ regions (from the W target) are listed in Table 23 and shown in Fig. 26 along with the CP data. Most of our data

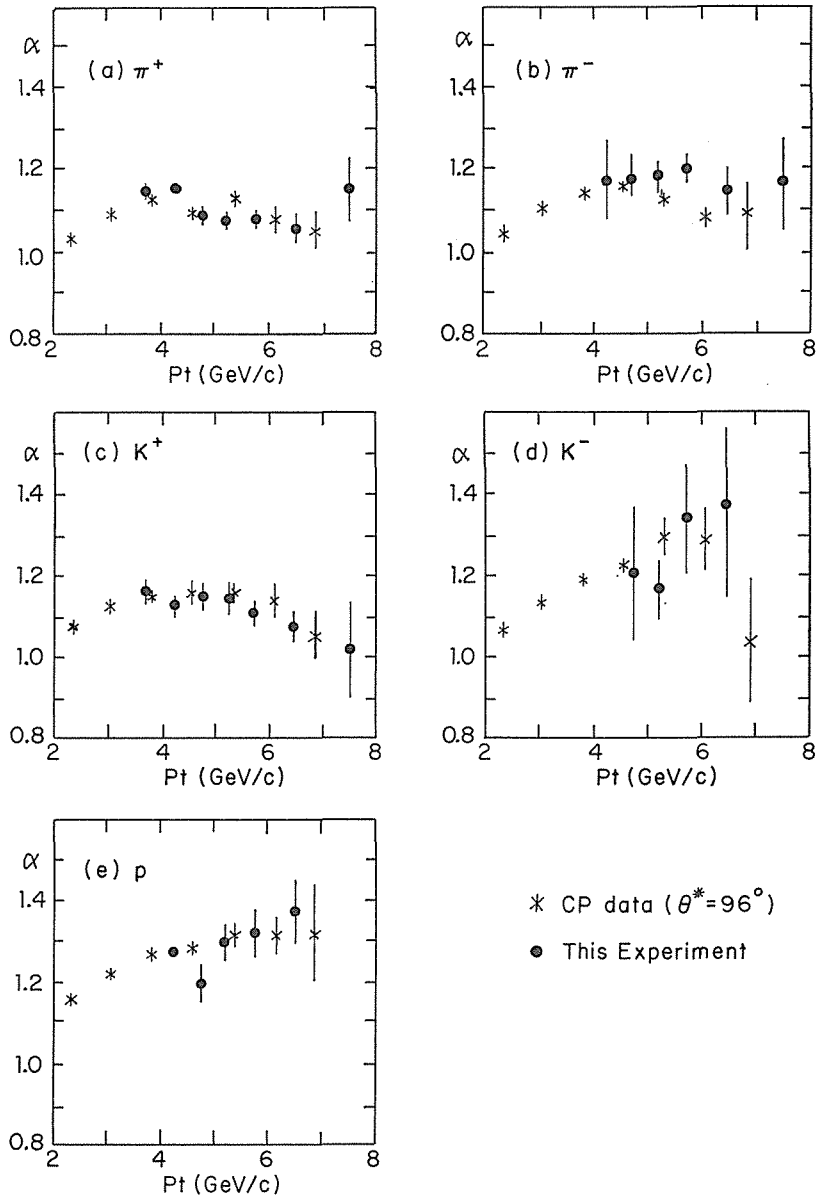


Fig. 27. $\alpha$ for each hadron type as a function of $P_t$.
(this experiment (●) and the CP measurement (×)).

are in a more forward region than the CP data, but two data sets agree well in the overlapping regions. The relative cross-section for the Be, Cu, and W targets are fit as in equation (19) and the values of the power $\alpha$ are evaluated. The results are listed in Tables 24 and 25, and are also shown in Figs. 27 and 28. The agreement with the CP data is good.

**Systematic Errors**

In addition to statistical errors listed in Tables 17 to 25, there are some systematic errors in calculating the $A$-dependence.

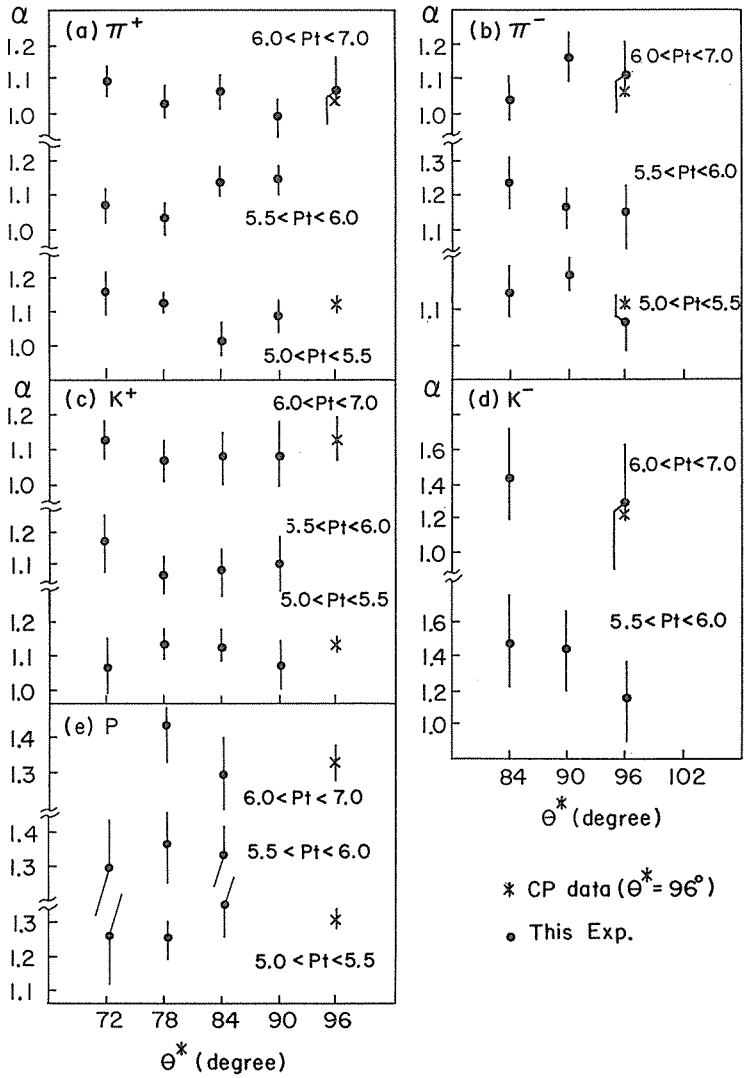


Fig. 28. $\alpha$ for each hadron type as a function of $\theta^*$.
(this experiment (◉) and the CP measurement (×)).

Table 21. The cross-section per nucleus for each hadron type for the Be and Cu targets relative to the W target as a function of $P_t$.

| Target | $Pt$(Gev/c) | $\pi^+$ | $K^+$ | $p$ | $\pi^-$ | $K^-$ |
|---|---|---|---|---|---|---|
| Be | 3.5∼4.0 | .0336±.0017 | .0327±.0030 | — — | — — | — — |
| | 4.0∼4.5 | .0329±.0008 | .0348±.0016 | .0204±.0011 | .0282±.0097 | — — |
| | 4.5∼5.0 | .0362±.0020 | .0322±.0034 | .0309±.0043 | .0316±.0043 | .0244±.0139 |
| | 5.0∼5.5 | .0401±.0020 | .0347±.0029 | .0209±.0026 | .0284±.0030 | .0284±.0087 |
| | 5.5∼6.0 | .0392±.0025 | .0347±.0036 | .0182±.0037 | .0286±.0036 | .0287±.0099 |
| | 6.0∼7.0 | .0435±.0031 | .0394±.0047 | .0171±.0046 | .0303±.0047 | .0134±.0111 |
| | 7.0∼8.0 | .0303±.0071 | .0501±.0157 | — — | .0269±.0085 | — — |
| Cu | 3.5∼4.0 | .286±.011 | .248±.018 | — — | — — | — — |
| | 4.0∼4.5 | .293±.005 | .315±.011 | .274±.009 | .355±.089 | — — |
| | 4.5∼5.0 | .307±.014 | .342±.027 | .261±.028 | .257±.029 | .297±.118 |
| | 5.0∼5.5 | .330±.014 | .295±.020 | .236±.018 | .294±.023 | .347±.079 |
| | 5.5∼6.0 | .315±.017 | .322±.026 | .250±.028 | .274±.027 | .175±.051 |
| | 6.0∼7.0 | .334±.021 | .329±.033 | .208±.032 | .329±.037 | .280±.140 |
| | 7.0∼8.0 | .299±.055 | .305±.087 | — — | .344±.079 | — — |

Table 22. The cross-section of each hadron type relative to pions for the Be, Cu, and W targets as a function of $P_t$.

| Target | $P_t$(Gev/c) | $K^+/\pi^+$ | $p/\pi^+$ | $K^-/\pi^-$ |
|---|---|---|---|---|
| Be | 3.5∼4.0 | .454±.039 | — — | — — |
| | 4.0∼4.5 | .445±.018 | .308±.018 | — — |
| | 4.5∼5.0 | .366±.037 | .293±.037 | .082±.041 |
| | 5.0∼5.5 | .424±.034 | .264±.031 | .142±.039 |
| | 5.5∼6.0 | .439±.043 | .181±.036 | .149±.050 |
| | 6.0∼7.0 | .411±.045 | .179±.040 | .037±.031 |
| Cu | 3.5∼4.0 | .405±.025 | — — | — — |
| | 4.0∼4.5 | .458±.013 | .478±.014 | — — |
| | 4.5∼5.0 | .459±.028 | .310±.029 | .122±.035 |
| | 5.0∼5.5 | .437±.025 | .329±.025 | .180±.030 |
| | 5.5∼6.0 | .506±.034 | .299±.030 | .119±.029 |
| | 6.0∼7.0 | .447±.036 | .315±.035 | .110±.030 |
| | 7.0∼8.0 | .471±.110 | .271±.098 | — — |
| W | 3.5∼4.0 | .467±.027 | .617±.031 | — — |
| | 4.0∼4.5 | .421±.012 | .503±.014 | — — |
| | 4.5∼5.0 | .412±.027 | .379±.031 | .111±.033 |
| | 5.0∼5.5 | .490±.028 | .471±.031 | .158±.028 |
| | 5.5∼6.0 | .495±.034 | .355±.033 | .185±.035 |
| | 6.0∼7.0 | .454±.039 | .514±.056 | .118±.033 |
| | 7.0∼8.0 | .461±.112 | .404±.115 | .069±.050 |

Table 23. The cross-section of each hadron type relative to pions as a function of $\theta^*$.

| | $P_t$(Gev/c) | polar angle in C.M.S. $\theta^*$ (degree) | | | | |
|---|---|---|---|---|---|---|
| | | 69~75 | 75~81 | 81~87 | 87~93 | 93~99 |
| $K^+/\pi^+$ | 3.5~4.0 | .537±.058 | .430±.029 | — — | — — | — — |
| | 4.0~4.5 | .469±.039 | .420±.014 | .403±.026 | — — | — — |
| | 4.5~5.0 | .541±.064 | .361±.034 | .485±.066 | .464±.235 | — — |
| | 5.0~5.5 | .424±.084 | .522±.042 | .478±.053 | .482±.067 | — — |
| | 5.5~6.0 | .509±.083 | .541±.069 | .497±.067 | .344±.065 | .507±.163 |
| | 6.0~7.0 | .448±.078 | .409±.059 | .525±.082 | .484±.105 | — — |
| $p/\pi^+$ | 3.5~4.0 | .718±.070 | .591±.039 | — — | — — | — — |
| | 4.0~4.5 | .505±.040 | .527±.017 | .454±.030 | — — | — — |
| | 4.5~5.0 | .443±.062 | .358±.036 | — — | — — | — — |
| | 5.0~5.5 | .436±.093 | .502±.044 | .597±.058 | .517±.087 | .496±.174 |
| | 5.5~6.0 | .360±.077 | .441±.059 | .452±.070 | .264±.066 | .425±.160 |
| | 6.0~7.0 | — — | .496±.071 | .456±.092 | — — | — — |
| $K^-/\pi^-$ | 4.5~5.0 | — — | — — | .126±.058 | .105±.041 | — — |
| | 5.0~5.5 | — — | — — | .119±.052 | .192±.038 | — — |
| | 5.5~6.0 | — — | — — | .207±.066 | .212±.055 | .093±.062 |
| | 6.0~7.0 | — — | — — | .125±.059 | .078±.040 | .172±.106 |

Table 24. The values of $\alpha$ for each hadron type as a function of $P_t$ for cross-section integrated over $\theta^*$.

| $P_t$ (Gev/c) | $\theta^*$ (degree) | $\pi^+$ | $K^+$ | $p$ | $\langle\theta^*\rangle$ (degree) | $\pi^-$ | $K^-$ |
|---|---|---|---|---|---|---|---|
| 3.5~4.0 | 76.2 | 1.134±.015 | 1.172±.029 | — — | — | — — | — — |
| 4.0~4.5 | 78.8 | 1.136±.007 | 1.109±.013 | 1.273±.011 | 86.2 | 1.156±.099 | — — |
| 4.5~5.0 | 78.2 | 1.102±.017 | 1.120±.031 | 1.191±.046 | 87.6 | 1.172±.043 | 1.216±.160 |
| 5.0~5.5 | 81.5 | 1.063±.015 | 1.121±.026 | 1.304±.036 | 90.2 | 1.176±.031 | 1.156±.089 |
| 5.5~6.0 | 82.2 | 1.076±.019 | 1.107±.031 | 1.321±.056 | 89.7 | 1.186±.038 | 1.349±.139 |
| 6.0~7.0 | 81.2 | 1.039±.022 | 1.069±.036 | 1.375±.079 | 90.7 | 1.142±.045 | 1.367±.220 |
| 7.0~8.0 | 81.2 | 1.156±.070 | 1.013±.095 | — — | 90.1 | 1.172±.090 | — — |

(a) Error in the background

As described in Sec. IV–D, a quadratic form for the background distribution is chosen for convenience. The error in $\alpha$ due to the estimation of the background distribution function is estimated to be around 0.01.

(b) Error in the relative number of protons on targets

As described in Sec. IV–E, the relative number of protons incident on the target is calculated from the total counts in the 90 degree monitor and the ratio of the 90 degree monitor to the SEM for each target. The errors in the ratios of the 90 degree monitor to the SEM are estimated to be 8.7, 12.9, and 9.6% for the Be, Cu, and W target, respectively. Possible errors in $\alpha$ due to this variation amount to 0.04.

Table 25. The values of $\alpha$ for each hadron type as a function of $\theta^*$ for different $P_t$ regions.

| hadron type | $\theta^*$ (degree) | $P_t$(Gev/c) | | |
|---|---|---|---|---|
| | | 5.0∼5.5 | 5.5∼6.0 | 6.0∼7.0 |
| $\pi^+$ | 69∼75 | 1.167±.057 | 1.070±.046 | 1.081±.048 |
| | 75∼81 | 1.107±.023 | 1.012±.033 | 1.017±.039 |
| | 81∼87 | 1.012±.025 | 1.124±.040 | 1.040±.041 |
| | 87∼93 | 1.069±.043 | 1.128±.047 | .991±.053 |
| | 93∼96 | — — | — — | 1.042±.098 |
| $K^+$ | 69∼75 | 1.075±.086 | 1.188±.074 | 1.105±.076 |
| | 75∼81 | 1.149±.036 | 1.055±.052 | 1.057±.061 |
| | 81∼87 | 1.133±.051 | 1.095±.057 | 1.095±.066 |
| | 87∼93 | 1.083±.081 | 1.102±.086 | 1.064±.093 |
| $p$ | 69∼75 | 1.275±.130 | 1.308±.139 | — — |
| | 75∼81 | 1.261±.051 | 1.378±.103 | 1.472±.123 |
| | 81∼87 | 1.376±.071 | 1.346±.094 | 1.307±.102 |
| $\pi^-$ | 81∼87 | 1.122±.069 | 1.240±.071 | 1.027±.069 |
| | 87∼93 | 1.212±.037 | 1.170±.051 | 1.141±.068 |
| | 93∼99 | 1.032±.064 | 1.151±.081 | 1.100±.098 |
| $K^-$ | 81∼87 | — — | 1.486±.241 | 1.432±.289 |
| | 87∼93 | 1.215±.107 | 1.465±.217 | — — |
| | 93∼99 | — — | 1.062±.295 | 1.276±.341 |

(c) Error in the particle identification efficiency

An error in the calculation of the particle identification efficiency of the Cherenkov counter cancels out for pions and kaons, but causes a systematic error in $\alpha$ for protons. This error is estimated to be 0.05.

Errors from other sources such as tracking efficiency correction are estimated to be negligibly small compared with the above errors. In summary, total systematic error of 0.065 and 0.041 should be to be added to the statistical error on $\alpha$ for protons and for the other particles, respectively.

## B. Discussion

As described earlier, models such as the multi-quark cluster model try to explain the $A$-dependence of single high $P_t$ hadron production by a dependence of the parton distribution on nuclear species. Assuming the parton picture is correct, the dependence of the parton distribution on the nuclear species should be directly observed in lepton-hadron deep inelastic scattering experiments. In fact, some dependence is observed by the EMC collaboration and the SLAC-MIT-Rochester group as described in Sec. I-D.

In these models, the nuclear dependence of the parton distribution found in the EMC effect must explain the $A$-dependence of single high $P_t$ hadron production. Therefore, the expected values of $\alpha$ for the single high $P_t$ hadron production from the models which include the EMC effect have been calculated and compared

with the present results. The following relation between $\alpha$ and the cross-sections on deuterium and iron is assumed in our calculation,

$$\alpha = \frac{\ln(\sigma_{Fe}/\sigma_D)}{\ln(A_{Fe}/A_D)} . \tag{20}$$

This relation has been confirmed by the CP group using their results on single high $P_t$ hadron production in which their deuterium target results agreed with extrapolation from other nuclear targets. In order to calculate the cross-section for single hadron production, the distribution of each type of parton must be known. Unfortunately the data on lepton-hadron deep inelastic scattering provide only ratios of the structure function $F_2$. Therefore, specific models must be used to extract each distribution function. Among the models described in the introduction, the CRR model (involving a change of confinement scale) and the averaged multicluster model (AMQC) model have been chosen for the following reasons;

i) Both models provide the distribution of each type of parton in a nucleus in a convenient form to calculate the cross-section for single hadron production.

ii) The two models represent two rather extreme cases. The AMQC model assumes that the nucleus contains extra components not present in a single nucleon. The CRR model assumes that some quantity such as the scale or size in a nucleus differs from that of a nucleon.

Result using other models would be more or less similar to either of these two models.

**CRR Model**

Close, Roberts, and Ross [43] argued in the context of QCD that the $A$-dependence of parton distributions arises as a result of the $A$-dependence of the scale of confinement in a nucleus. By expressing the relation between the structure function of deuterium and iron as,

$$F_2^{Fe}(x, Q^2) = F_2^D(x, \xi Q^2) , \tag{21}$$

they found that $\xi$ is not sensitive to $Q^2$ and $\xi=2$ gives good agreement with the EMC data. The authors pointed out that the above scale change does not reproduce the EMC data exactly, but rather their model explains the trend of the data. Nevertheless, this model is based on a well understood QCD calculation. In order to calculate the cross-section for single hadron production, a QCD calculation based on the Field-Feynman model [10] is used. The parametrization by R. Baier [62] was used for the $Q^2$ dependent parton distribution functions and fragmentation functions. We used $\Lambda=0.27$ Gev$^2$ as suggested by CRR. The rise of the ratio of the structure functions $F_2$ in the high $x$ region shown by the SLAC-MIT-Rochester data can not be reproduced with these functions alone. A. Bodek et al [34] made a calculation including the Fermi motion of nucleons in an iron nucleus and the result gives the rise of the ratio in the high $x$ region as shown in Fig. 6. In our calculation, the effects due to the Fermi motion are also folded in following the simple

method discussed by J. Kuhn [23] who calculated the effect of Fermi motion in single high $P_t$ hadron production. The CRR model including Fermi motion reproduces the data on $F_2^{Fe}/F_2^D$ in the whole $x$ region. Cross-sections for single high $P_t$ hadron production were calculated as a function of $P_t$ at $\theta^*=90$ degrees, and as a function of $\theta^*$ at $P_t=4.75$ Gev/c.

**Averaged Multi-quark Cluster Model**

In the multi-quark cluster model, the parton distribution function in the nucleus is replaced with a sum of distribution functions of the multi-quark states;

$$G_{a/\text{Nucleus}}(x) = \sum_{i=1}^{A} n_i^A \tilde{G}_{a/3i}(x) \tag{22}$$

where $n_i^A$ is the expectation value of the number of $3i$-quark states in the nucleus. The $\tilde{G}_{a/3i}(x)$ must satisfy the following sum rules;

$$\begin{aligned} &\sum_a \int_0^i x\tilde{G}_{a/3i}(x)\mathrm{d}x = 1 \\ &\sum_a \int_0^i \tilde{G}^v_{a/3i}(x)\mathrm{d}x = 3i\,, \end{aligned} \tag{23}$$

where $\tilde{G}^v_{a/3i}(x)$ is the distribution function of valence quarks. In order to calculate the structure function of the nucleus, $n_i^A$ and $\tilde{G}_{a/3i}(x)$ must be known.

J. deDeus [36] made a calculation by parametrizing nuclear structure functions using the average number of nucleons per cluster. In this calculation, the structure function is expressed as follows;

$$F_2^A(x) = f\cdot(\eta_i+1)\cdot\left(1-\frac{x}{\langle i\rangle}\right)^{\eta_i}, \tag{24}$$

where $\langle i\rangle$ is the average number of nucleons per cluster. By fitting the data, $\langle i\rangle$ and $\eta_i$ were found to be 1 and 3.5 for deuterium and 1.08 and 2.75 for iron, respectively. The valence quark distribution was parametrized as;

$$x\cdot G_{v/A}(x) = \frac{\langle i\rangle}{B(\alpha_i,\ \beta_i+1)}\left(\frac{x}{\langle i\rangle}\right)^{\alpha_i}\left(1-\frac{x}{\langle i\rangle}\right)^{\beta_i}, \tag{25}$$

where $B$ is the beta function to normalize $G_{v/A}(x)$ to $\langle i\rangle$. The sea quark distribution function was calculated from $F_2$ and $G_{v/A}$, assuming an SU(3) symmetric sea. This provides a sea quark enhancement for iron. The gluon distribution function $G_{g/A}(x)$ was taken from Ref. 8, as follows;

$$x\cdot G_{g/A}(x) = g_i\cdot\left(1-\frac{x}{\langle i\rangle}\right)\cdot\left(1-\frac{x}{\langle i\rangle}\right)^4. \tag{26}$$

The normalization of each component for deuterium was arranged so that the fraction of momentum carried by the sea, valence quarks, and gluons was 15%, 30%, and 55%, respectively. The parameters used are listed in Table 26. The $Q^2$

Table 26. The parameters used in the averaged multi-quark cluster model calculation.

| | | Deuterium | Iron |
|---|---|---|---|
| $\langle i \rangle$ | | 1. | 1.08 |
| $F_2$ | $f$ | .1167 | .1167 |
| | $\eta_i$ | 2.75 | 3.5 |
| Valence quark | $\beta_i$ | 3. | 3.8 |
| | $\alpha_i$ | .444 | .490 |
| Gluon | $g_i$ | 1.096 | 1.914 |

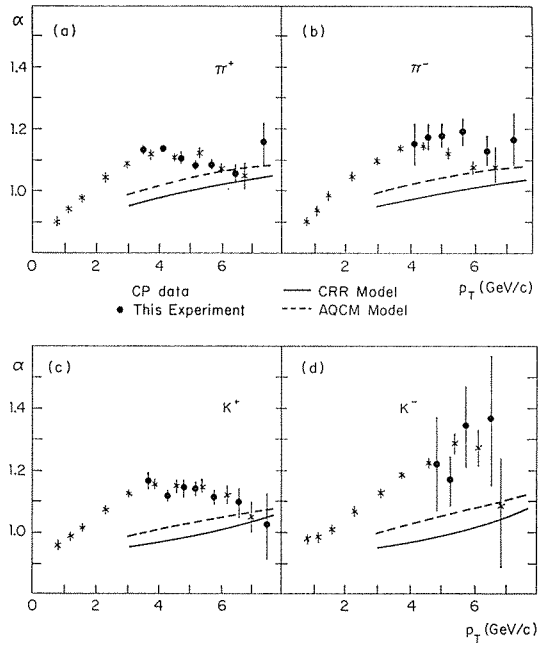


Fig. 29. Comparison of $\alpha$ predicted by the CRR model (---) and the AMQC model (——) with data as a function of $P_t$ at 90 degrees in C.M. system.
(this experiment (●) and the CP measurement (×)).

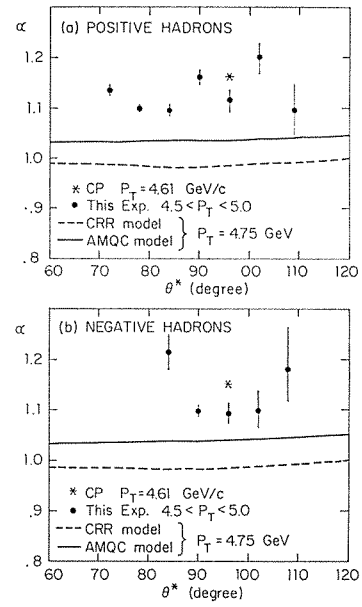


Fig. 30. Comparison of $\alpha$ predicted by the CRR model (---) and the AMQC model (——) with data as a function of $\theta^*$ at $P_t$=4.5 Gev/c.
(this experiment (●) and the CP measurement (×)).

dependence of the distribution functions was not taken into account. Since this parametrization includes the rise of the ratio in the high $x$ region, only the transverse component of the Fermi motion which give a negligible effect on $\alpha$ was incorporated.

The results of our calculations using the two models are shown in Fig. 29 and 30. The lack of $\theta^*$ dependence of $\alpha$ indicated by the data is well reproduced by the two models. However, both models fail to explain the $P_t$ dependence of $\alpha$

in the $P_t$ range 3 to 5 Gev/c for $\pi^{\pm}$ and $K^+$. For $K^+$, the discrepancies are large and almost everywhere.

Date et al argued both single high $P_t$ hadron production [27] and the EMC effect [35] within the multi-quark cluster model in a more sophisticated way from the theoretical side. In the calculation, $\tilde{G}_{a/3i}(x)$ is obtained by using an extension of the modified Kuti-Weisskopf model [59]. The parameters are determined so that $\tilde{G}_{a/3i}(x)$ is equal to the parton distribution function of the nucleon when $A$ is equal to 1. Since there is no theory to predict $n_i^A$, it was parametrized as follows;

$$n_i^A \propto \binom{A}{i} p(A)^{i-1} \cdot (1-p(A))^{A-1}, \tag{27}$$

where $p(A)$ is a parameter to be determined by fitting the experimental. They showed good agreement with data for single high $P_t$ hadron production in contrast to our result. However, their predictions for the EMC effect give a ratio of structure functions which already exceeds 1 at $x=0.7$, while the data show that the ratio is almost minimum and does not exceed 1 until around $x=0.85$.

According to our calculations, it seems unlikely that the difference of the structure functions between nuclei can explain the $A$-dependence of single high $P_t$ hadron production. Therefore, some other mechanism which is not seen in lepton-hadron deep inelastic scattering is required to explain the $A$-dependence of single high $P_t$ hadron productions.

One such candidate is the multiple scattering model. Recently calculations based on the QCD parton model have been made by Kryzwicki et al [24] and Lev et al [25]. They use $Q^2$ dependent parton distribution functions and fragmentation functions extracted from experimental results [60]. They regularized the singularities by adding 1 Gev$^2$ to $\hat{s}$, $\hat{t}$, and $\hat{u}$ in the denominators, since the cross-section for the QCD elementary sub-processes has singularities. Their results reproduce the data well, even the difference in $\alpha$ between $K^-$ and other mesons. In their model, these difference can be explained by the enhancement of gluons in multiple scattering. In the QCD sub-processes, diagrams involving the gluon self-coupling have a bigger cross-section by the color factor 9/4 than those with quark-gluon coupling only, as seen in Table 1. Therefore, in double or higher multiple scattering, this color factor enhances the contribution of gluons relative to quarks. In a proton-nucleus scattering, $\pi^{\pm}$ and $K^+$ are mainly produced by valence quarks. On the other hand $K^-$ production is dominated by the contribution of gluons, since none of the valence quarks in $K^-$ are included in the beam proton or target nucleus as valence quarks. Hence the $\alpha$ for the $K^-$ production must be bigger than $\alpha$ for $\pi^{\pm}$ and $K^+$ production.

## C. Conclusion

Measurements on the atomic weight dependence of single high $P_t$ hadron production, $a$, have been extended up to 8 Gev/c in $P_t$, and from 70 to 110 degrees in polar angle in the C.M. system. No significant dependence on the polar angle

was observed and the observed $P_t$ dependence of $\alpha$ was consistent with the previous experiments.

A difference in structure functions for different nuclei used by the multi-quark cluster model proponents to reproduce the observations of the EMC collaboration and the SLAC-MIT-Rochester group is not a likely explanation of the $A$-dependence of single high $P_t$ hadron productions. Contribution of other mechanisms such as in the multiple scattering model is necessary.

## ACKNOWLEDGMENTS

The author would like to express his sincere thanks to his advisor, Prof. K. Miyake, and to Prof. A. Maki and Dr. Y. Hemmi for their continuous encouragement and guidance throughout this work. He is deeply grateful to Dr. C. Brown, the spokesman of the experiment, and to each member of the E605 group for their advice and collaboration in carrying out this experiment:
C. Brown, S. Childress, D. Finley, A. Ito, A. Jonkheere, H. Jostlein, L. Lederman, R. Orava, S. Smith, K. Sugano, K. Ueno (FNAL); R. McCarthy, M. Adams, G. Coutrakon, H. Glass, D. Jaffe, J. Kirz (Stony Brook); K. Young, J. Rutherfoord, J. Rothberg, R. Williams, R. Gray, R. Plaag (Washington); D. Kaplan, J. Crittenden, Y. Hsiung (Columbia); J.R. Hubbard, Ph. Mangeot, A. Peisert (Saclay); G. Charpak, F. Sauli (CERN); A. Maki (KEK); K. Miyake, T. Nakamura, Y. Hemmi, K. Imai, N. Sasao, N. Tamura, T. Yoshida (Kyoto).

Thanks especially go to Y. Hsiung, J. Crittenden, and H. Glass, my fellow graduate students, for working together on the software analysis and for many useful discussions.

He would like to thank Mr. R. Krull who worked on the construction of the calorimeter, and all the other technicians involved in this experiment for working on the construction of the various detectors.

He is indebted to the personnel at FNAL, the members of the accelerator crew for stable operation of the proton synchrotron, the switch yard group for tuning and operating the beam line, the Meson experimental area department for supporting the construction of the experimental apparatus, the PREP group for providing the necessary electronics, the computer division for assistance in off-line data analysis, and many others.

Finally he would like to express his sincere thanks to Japan-U.S.A. collaboration program for giving him the opportunity to work on the present experiment in U.S. Thanks are also due to the Universities Research Association, Inc. and the Japan Society for the Promotion of Science for their financial support.

## APPENDIX I. SCINTILLATOR AND WAVE LENGTH SHIFTER

Since our calorimeter needed to have a large acceptance, a large volume of scintillator was required (around 3.6 tons in total). If an ordinary plastic scintillator such as NE110 was used, the calorimeter would be very expensive. There have been many other types of acrylic scintillators for this reason [61]. New types

of inexpensive scintillators with a PMMA (polymethylmethacrylate) base have been used in calorimeters recently [62]. In order to decide which scintillator to use, several types of scintillator, including some newly developed by Japanese companies, and NE110 were measured. Those scintillators are listed in Table 27. The light yield produced by cosmic rays from the sample scintillators (20 cm × 150 cm × 6 mm) was measured using the same phototube. The attenuation along the scintillator was also measured. The yield of photo electrons was estimated from the width of the charge distribution. Fig. 31 shows the results for the case in which the phototube was directly attached to the scintillator with optical grease (for EM part). For the hadron part, wave length shifter (WLS) bars were used to collect the light and to simplify the construction. For several combinations of scintillator and WLS bars, the light yield was measured. In this case, the light was collected through the WLS bar which was coupled to the scintillator with a small air gap and which was attached to the phototube with optical grease. The results are shown in Fig. 32. The final selection was based on the following points.

i) A large light output, especially with the WLS bars, because in the WLS bar coupled case the light output is expected to be smaller by an order of magnitude than the direct coupled case.

ii) Small attenuation along the scintillator. The attenuation could be corrected in the off-line analysis because the chambers provide the hit position in the calorimeter. However, small attenuation was important to achieve a more uniform trigger.

Kyowa SCAS1101 gave high performance for both criteria and was selected. SCAS1101 scintillator is made of 50% polystylene and 50% PMMA, and contains no naphthalene in contrast to the other acrylic scintillators. The SCAS1101 scintillator gives a light yield about 80% of NE110 and is mechanically as strong as acrylic scintillators. For the WLS bar, Altulor 1290 was selected because of its small attenuation and high efficiency.

Table 27. Specifications of various scintillators.

| Company | Name | Base | Solutions | Price ($) (for 3.6 ton) |
|---|---|---|---|---|
| Rohm | 1921 | PMMA | Naphthalene(1%)+Butyl-PBD(1%)+POPOP(.01%) | |
| | 1922 | PMMA | Naphthalene(3%)+Butyl-PBD(1%)+POPOP(.01%) | 66K |
| | 2003 | PMMA | Unknown | 161K |
| Kyowa | SCAS0101 | PMMA(50%)+Polystylen(50%) | Butyl-PBD(1%)+POPOP(.01%) | |
| | SCAS1101 | PMMA(50%)+Polystylen(50%) | Butyl-PBD(1%)+POPOP(.02%) | 68K |
| Sumitomo | SC-5 | PMMA | Naphthalene( 1%)+PPO(1%)+POPOP(.01%) | 48K |
| | SC-12 | PMMA | Naphthalene(10%)+PPO(1%)+POPOP(.01%) | 66K |
| | SC-18 | PMMA | Naphthalene(10%)+Butyl-PBP(1%)+BBOT(.01%) | 107K |
| Altustipe | BLUE | PMMA | Naphthalene(15%)+Butyl-PBD(1%)+BBOT(.01%) | 55K |
| | YELLOW | PMMA | Naphthalene(15%)+Butyl-PBD(1%)+BBQ(.0025%) | 68K |

note) The names of the scintillators of Kyowa and Sumitomo are not commercial ones.

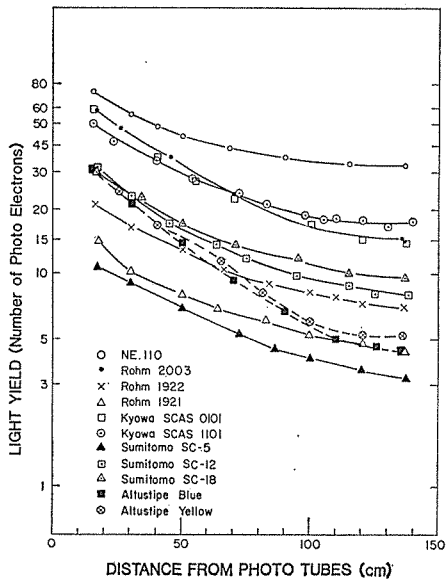


Fig. 31. Light yields for minimum ionizing particles for various scintillators in the direct coupling case.
The scintillators were wrapped with aluminized mylar. The curves serve to guide the eyes.
The data points are (○) NE110, (●) Rohm 2003, (×) Rohm 1922, (△) Rohm 1921, (□) Kyowa SCAS0101, (⊙) Kyowa SCAS1101, (▲) Sumitomo SC-5, (⊡) Sumitomo SC-12, (△) Sumitomo SC-18, (■) Altustipe Blue, and (⊗) Altustipe Yellow.

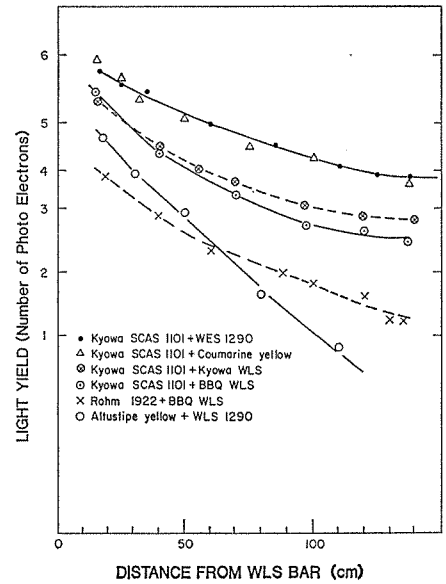


Fig. 32. Light yields for minimum onizing particles for various combinations of scintillator and wave length shifter bar.
The size of the wave length shifter bars were,
BBQ WLS; 20 cm×12 cm×3 mm,
Altulor 1290, Kyowa WLS, and
Coumerin yellow; 20 cm×20 cm×6 mm.
The data points are;
●: Kyowa SCAS1101+WLS 1290,
▲: Kyowa SCAS1101+Coumerin yellow,
⊗: Kyowa SCAS1101+Kyowa WLS,
⊙: Kyowa SCAS1101+BBQ WLS,
×: Rohm 1922+BBQ WLS,
○: Altustipe Yellow+WLS 1290.

## APPENDIX II. TRACE BACK AND MOMENTUM ANALYSIS

### A. SM12 Magnetic Field and Trace Back

Since the shape of the pole piece inserts in the SM12 magnet is complicated, the shape of the field is also complicated and it is difficult to parametrize the entire magnetic field of the SM12 magnet. To avoid this complexity, we divided the SM12 magnet into 36 sub-magnets along the $z$ direction. The length of these sub-magnets is chosen to be the same as the step length of the pole pieces (45.7 cm), except for the last few sub-magnets in the fringe field region. For each sub-magnet, the integral of the magnetic field along the line approximately pointing at the target in the $x$–$z$ plane is given as a function of $x$ and $y$. This quantity determines the bend angle of the particles ($P_t$ kick). Equation (19), used for the SM3 magnet, is also used for the sub-magnets of SM12. The $z$ position of the effective bend

plane of each sub-magnet is also given as a function of $x$ and $y$. The following function is used;

$$z_{\mathrm{BEND}}(x, y) = a_0+a_1x^2+a_2y^2+a_3x^2y^2 . \tag{28}$$

The trajectory of particles downstream of the SM3 magnet is traced back to the target through the SM3 magnet and the SM12 magnet. The trace back in the sub-magnets is made using the single bend plane approximation with an $x$, $y$ dependent $P_t$ kick and bend plane.

**B. Recalculation of the Momentum**

At first, the trace back is done using the 'SM3 momentum'. For trajectories whose $y$ position at the target is within acceptable limits, the momenta and trajectories are then recalculated assuming that the trajectories originate from the center of the target in the following manner.

The $y$ position at the target for the first trace back using the 'SM3 momentum' (denoted as $p_0$) is given by,

$$\begin{aligned} y_T(p_0) &= y_{M3}+\theta_y\cdot(z_T-z_{M3})+\frac{II(p_0)}{p_0} , \\ II(p) &= \int_{z_{M3}}^{z_T} \mathrm{d}z \int_{z_{M3}}^{z_T} \mathrm{d}z' B_x(z') , \end{aligned} \tag{29}$$

where $z_T$, $z_{M3}$=the $z$ positions at the center of the target and at the bend plane of the SM3 magnet, respectively,

$y_T$, $y_{M3}$=the $y$ position of the trajectory at $z=z_T$ and $z_{M3}$, respectively,

$\theta_y$ =the angle of the trajectory downstream of SM3 in the $y-z$ plane,

$B_x$=the horizontal component of the magnetic field at position $z$.

If the trajectory is traced back using a slightly different momentum, say $p_0+\mathrm{d}p$, then the $y$ position at the target would be given by,

$$\begin{aligned} y_T(p_0+\mathrm{d}p) &= y_T(p_0)-\left[\frac{II(p_0)}{p_0^2}-a(p_0)\right]\cdot \mathrm{d}p , \\ a(p_0) &= \frac{1}{p}\frac{\mathrm{d}II}{\mathrm{d}p}\bigg|_{p=p_0} . \end{aligned} \tag{30}$$

The value of $II(p_0)$ is calculated in the first trace back, while $a(p_0)$ is unknown but is expected to be small. Neglecting $a(p_0)$, the momentum with a target constraint is given by equating $y_T(p_0+\mathrm{d}p)=Y_{\mathrm{traget}}$,

$$p_1 = p_0+\mathrm{d}p = p_0+\frac{II(p_0)/p_0^2}{y_T(p_0)-y_{\mathrm{target}}} , \tag{31}$$

where $y_{\mathrm{target}}$ denotes the $y$ position of the target center. Then a second trace back is made using the momentum $p_1$. Using the $y$ position at the target $y_T(p_1)$ obtained from the second trace back, one can evaluate the momentum with a target constraint including the term $a(p_0)$ as follows;

$$p_2 = p_0 + \frac{y_T(p_0) - y_{\text{target}}}{y_T(p_0) - y_T(p_1)} \cdot (p_1 - p_0) \,. \tag{32}$$

The value $p_2$ is taken as the final 'SM12 momentum'. In the above calculation, terms of order $dp^2$ are neglected. These terms prove to be negligibly small in our case, because $y_T(p_2)$ calculated using the momentum $p_2$ coincides with $y_{\text{target}}$ almost exactly. Other quantities, such as the production angle and the position of the trajectory at aperture points are then evaluated in the same way as the momentum $p_2$.

## References


1. A. Bodek et al, Phys. Rev. Lett. **30**, 1987 (1973)
   J.S. Poucher et al, Phys. Rev. Lett. **32**, 118 (1974)
2. For a review of parton models and "hard processes", see for example;
   R.P. Feynman, "Photon-Hadron Interactions", W.A. Benjamin, Inc. (1972)
   F.E. Close, "An Introduction to Quarks and Partons", New York Academic Press (1979)
   W.B. Atwood, Lectures given at the Summer Institute on Particle Physics, 7th, SLAC (1979), p1-114 in "Lectures on Lepton Nucleon Scattering and Quantum Chromodynamics", Birkhauser, Boston (1982)
3. R.D. Field and R.P. Feynman, Phys. Rev. **D15**, 2590 (1977)
   R.P. Feynman, R.D. Field, and G.C. Fox, Nucl. Phys. **B128**, 1 (1977).
4. B. Blankenbecler, S.J. Brodsky, and J.F. Gunion, Phys. Rev. **D12**, 3469 (1975).
5. H.D. Polizer, Phys. Rev. Lett. **30**, 1346 (1973).
   D.J. Gross and F. Wilczek, Phys. Rev. **D8**, 3633 (1973), Phys. Rev. **D9**, 980 (1974).
   H.D. Polizer, Phys. Report **14**, 129 (1974).
   For a review, see for example; A.J. Buras, Rev. of Mod. Phys. **52**, 119 (1980).
6. G. Altarelli and G. Parisi, Nucl. Phys. **B126**, 298 (1977).
7. B.L. Combridge, J. Kriphganz, and J. Ranft, Phys. Lett. **70B** 234 (1977).
8. For the extension of the "black box" model in a QCD framework see;
   R.D. Field, Phys. Rev. Lett. **40**, 997 (1978).
   R.P. Feynman, R.D. Field, and G.C. Fox, Phys. Rev. **D18**, 3320 (1978).
   R.D. Field, Phys. Rev. **D27**, 546 (1983).
9. For the extension of the CIM within QCD see;
   D. Jones, and J.F. Gunion, Phys. Rev. **D19**, 867 (1979).
   However a recent experiment in a pion beam shows a disagreement with the CIM, see H.J. Frish et al, Phys. Rev. Lett. **44**, 511 (1980), and also Ref. 20.
10. G. Bellettini et al, Nucl. Phys. **79**, 609 (1966)
    S.P. Denisov et al, Nucl. Phys. **B61**, 62 (1973).
11. J.W. Cronin et al, Phys. Rev. **D11**, 3105 (1975).
12. U. Becker et al, Phys. Rev. Lett. **37**, 1731 (1976).
13. D.A. Garbutt et al, Phys. Lett. **67B**, 355 (1977).
14. C. Bromberg et al, Phys. Rev. Lett. **42** ,1202 (1979).
15. R.L. McCarthy et al, Phys. Rev. Lett. **40**, 213 (1978).
    H. Jostlein et al, Phys. Rev. **D20**, 53 (1979).
16. D.A. Finley et al, Phys. Rev. Lett. **42**, 1031 (1979).
17. L. Kluberg et al, Phys. Rev. Lett. **38** 670 (1977).
    D. Antreasyan et al, Phys. Rev. **D19**, 764 (1979).
18. H.J. Frish et al, Phys. Rev. **D27**, 1001 (1983).
19. G. Berland, A. Dar, and G. Eilam, Phys. Rev. **D13** ,161 (1976).
    S. Fredriksson, Nucl. Phys. **B111**, 167 (1976).
20. J. Pumplin and E. Yen, Phys. Rev. **D11**, 1812 (1975).
    G.R. Farrar, Phys. Lett. **56B**, 185 (1975).

P. Fishbane, J.K. Kotsonis, and J.S. Trefil, Phys. Rev. **D16**, 122 (1977).
21. J.H. Kuhn, Phys. Rev. **D13**, 2949 (1976).
22. M.J. Longo, Nucl. Phys. **B134**, 82 (1978).
23. C. Michael and D.M. Weber, Phys. Lett. **83B**, 243 (1979).
24. A. Kryzwicki, J. Engels, B. Petersson, and U. Sukhatme, Phys. Lett. **85B**, 407 (1979).
25. M. Lev and B. Petersson, Z. fur Phys. **C21**, 155 (1983).
26. A. Krzywicki, Phys. Rev. **D14**, 152 (1976).
27. S. Date and A. Nakamura, Prog. Theor. Phys. **69**, 565 (1983).
28. J.J. Aubert et al, Phys. Lett. **123B**, 275 (1983).
29. A. Bodek et al, preprint SLAC-PUB-3041 (1983).
A. Bodek et al, preprint University of Rochester UR852 (1983).
30. A. Bodek and J.L. Ritchie, Phys. Rev. **D23**, 1070 (1980), Phys. Rev. **D24**, 1400 (1981).
31. L.L. Frankfurt and M.I. Strikman, Nucl. Phys. **B181**, 22 (1981).
G. Berland, A. Dar, and G. Eilam, Phys. Rev. **D22**, 1547 (1980).
32. For a review see;
K. Rith, Freiburg University preprint, THEP 83/4 (1983) (to appear in the Proceedings of the XVIII Recontre de Moriond 1983).
C.H. Llewellyn Smith, Oxford University preprint, 37/83 (1983).
33. J. Szwed, Phys. Lett. **128B**, 245 (1983).
34. R.L. Jaffe, Phys. Rev. Lett. **50**, 228 (1983).
H. Faissner and B.R. Kim, Phys. Lett. **130B**, 321 (1983).
W. Furmanski and A. Krzywicki, Orsay preprint LPTHE 83/11 (1983).
35. S. Date, to be published in Phys. Lett.
36. J.D. deDeus, preprint MPI-PAE/PTh 61/83 (1983).
37. O. Nachatman and H.J. Pirner, University of Heiderberg pr9print HD-THEP-83-8 (1983)
38. C.H. Llewellyn Smith, Phys. Lett. **128B**, 107 (1983).
M. Ericson and A.W. Thoman, Phys. Lett. **128B**, 112 (1983).
39. F.E. Close, R.G. Roberts, and G.G. Ross, Phys. Lett. **129B**, 346 (1983).
40. S. Fredriksson, Royal Institute of Technology preprint TRITA-TFY-83-15 (1983).
41. J. Cleymans, and J. Geris, University of Bielefeld preprint, BI-TP 83/16.
42. A.S. Ito et al, Phys. Rev. **D23**, 604 (1981).
43. K.J. Anderson et al, Phys. Rev. Lett. **42**, 944 (1979).
44. J. Badier et al, Phys. Lett. **104B**, 335 (1981).
45. S. Falciano et al, Phys. Lett. **104B**, 416 (1981).
46. J. Crittenden, Ph.D. Thesis, Columbia University, New York.
47. H. Glass, Ph.D. Thesis, State University of New York at Stony Brook.
48. E605 Proposal, Columbia-FNAL-Stony Brook Collaboration (May 1978).
Addendum to Proposal E605, L.M. Lederman et al (Nov 1978).
49. R.W. Fast et al, FNAL technical memo, TM-1034.
50. After the first running period, a photon shower Monte Carlo using the EGS program showed that the thickness of the brick (18 radiation lengths) was not thick enough to absorb the shower. It absorbed almost all the energy but a large number of low energy photons could escape from the back of the brick.
51. Y. Sakai et al, IEEE Transactions on Nuclear Science Vol. **NS-28**, 528 (1981).
52. S. Iwata, "Calorimeter", Nagoya Univ. preprint DPNU-13-80 (1980).
H. Whiteside et al, Nucl. Instr. and Meth. **109**, 375 (1973).
L.W. Jones et al, Nucl. Instr. and Meth. **118**, 431 (1974).
M. Holder et al, Nucl. Instr. and Meth. **151**, 69 (1978).
53. H. Glass et al, IEEE Transactions on Nuclear Science Vol. **NS-30**, 30 (1983).
M. Adams et al, Nucl. Instr. and Meth. **217**, 237 (1983).
54. J.R. Hubbard et al, Nucl. Instr. and Meth. **176**, 233 (1980).
R. Bouclier et al, Nucl. Instr. and Meth. **205**, 403 (1983).
55. J. Crittenden et al, to appear in IEEE Transactions on Nuclear Science.
56. R. Raja, FNAL technical memo, TM-1083 (1983).
57. G. Coutrakon et al, IEEE Transactions on Nuclear Science **NS-29**, 323 (1982).

58. R. Baier, J. Engels, and B. Petersson, Z. fur Phys. **C2**, 265 (1979).
59. J. Kuti and V.F. Weisskopf, Phys. Rev. **D4**, 3418 (1971).
60. J.H. Groot et al, Z. fur Phys. **C1**, 143 (1979).
61. W. Kienzle et al, European Organization for Nuclear Research, Internal Report 75-12 (1975).
J.A. Appel et al, FNAL note FN-313 (1978).
L. Allemand et al, Nucl. Instr. and Meth. **164**, 93 (1979).
J.C. Thevenin et al, Nucl. Instr. and Meth. **169**, 53 (1980).
G. Aurouet et al, Nucl. Instr. and Meth. **169**, 57 (1980).
62. E. Locci et al, Nucl. Instr. and Meth. **164**, 97 (1979).
H. Abramowicz et al, Nucl. Instr. and Meth. **180**, 429 (1981).
P. Rapp et al, Nucl. Instr. and Meth. **188**, 285 (1981).